Robotica (2022), **40**, pp. 951–975
doi:10.1017/S0263574721000874

CAMBRIDGE
UNIVERSITY PRESS

RESEARCH ARTICLE

Improving the performance of parallel robots by applying distinct hybrid control techniques

André G. Coutinho and Tarcisio A. Hess-Coelho*

Mechatronics and Mechanical Systems Engineering Department, Escola Politécnica, University of São Paulo, São Paulo, Brazil
*Corresponding author. E-mail: tarchess@usp.br

Received: 11 December 2020; **Revised:** 2 May 2021; **Accepted:** 9 June 2021; **First published online:** 27 July 2021

Keywords: parallel mechanisms; robotics; non-linear control; robust control; hybrid control

Abstract

During the last two decades, parallel robots have become more ubiquitous, employed in a great variety of sectors, from food to aerospace industries. In fact, they are much more efficient than their serial counterparts in terms of performing fast motions and consuming less energy. However, due to their mechanical complexity, they present a highly complex non-linear dynamics, which makes the modelling and control tasks difficult. Aiming to improve the performance and robustness of the control laws already used to control this type of mechanisms, this paper proposes two hybrid control techniques. The first hybrid control is derived from the combination of a pure PD control with a modified Sliding Mode control. The second hybrid control, in its turn, combines a pure Computed Torque with the altered Sliding Mode control. The proposed modifications in the Sliding Mode control aim to achieve a considerable reduction of the tracking errors and chattering. A stability analysis of the proposed control techniques and an experimental validation are carried out, comparing the performance of the pure and hybrid control laws in a 5R parallel mechanism. Moreover, simulations are also conducted to evaluate the behaviour of a 3-dof spatial parallel robot, when performing a 3D-path. Analysing the simulations and the experimental results, it is possible to observe a significant reduction of the path tracking and steady-state errors in both hybrid control strategies.

1. Introduction

1.1. Literature review

During the last two decades, parallel robots have become more ubiquitous, employed in a great variety of sectors, namely, food [1], medical [2], aerospace [3, 4] and agricultural [5]. Due to the modularity of their kinematic chains, the actuators can be installed at or near the fixed base, reducing the inertia of their mechanical structure. As a consequence, parallel robots are much more efficient than their serial counterparts in terms of performing fast motions and consuming less energy [6–8].

Concerning the control, the followed direction [9–11] has been to adapt the mature control techniques, already employed in most of serial robots, into the parallel ones. With respect to the decentralized control, the input signal for the control of an individual joint relies on the measurement of the related joint displacement and velocity [12]. According to Chung et al. [12], the decentralized control, such as the PID compensator, is appropriate in set-point regulation tasks. However, in operations that demand the capability of trajectory tracking and high speed, the PID performance is not satisfactory. In such cases, the centralized control, based on the robot dynamic model, considering the interaction between the active joints, can provide better results [9].

Among the investigated centralized control strategies, the Computed Torque techniques are certainly relevant due to the fact they convert a system, originally non-linear and coupled regarding the input and output variables, into a linear and decoupled closed-loop system. [12, 13] To succeed on applying such technique, one has to keep the model uncertainties under limited boundaries. [14] Among those, one can

© The Author(s), 2021. Published by Cambridge University Press.

https://doi.org/10.1017/S0263574721000874 Published online by Cambridge University Press

mention parameter uncertainties, load variations, model simplifications, friction, clearances and elastic deformations. [9, 15, 16]

For parallel robots, some critical factors play a significant role. First, the complexity of the complete inverse dynamics model [17, 18], characterized by the presence of a huge number of terms, may cause the infeasibility of the real-time control once their calculation is a compute-intensive task. In fact, this is a direct consequence of their mechanical structure due to the presence of more than a single kinematic chain and, consequently, moving bodies. Second, once the control is usually performed in the joint space, the path tracking error increases considerably mainly because of the existence of joint clearances, link deformations or even vibrations. On the other hand, the control in the task space has been employed; [19, 20] however, there are precision and cost limitations on the current available sensors to determine the end-effector location [21].

In order to overcome such drawbacks, some works propose the Computed Torque control in a feed-forward mode [10, 22, 23] because it allows the model computation out of the control loop. Moreover, others recommend the utilization of either robust or even adaptive control strategies [24–31] which have demonstrated promising results for parallel robots [9, 18, 26, 32, 33]. Among the robust approaches, the Sliding Mode (SM) control can deal with system model inaccuracies, parametric uncertainties and external disturbances [34]. The SM control drives the state trajectory to a predefined sliding surface by using discontinuous control inputs and retains it there [35]. However, this technique also shows some drawbacks, namely, chattering [36, 37], long settling time [36], non-smooth control input [35] and low tracking performance [38].

In order to overcome the limitations of each control technique and keep its own benefits, the hybrid control, that is, the combination of distinct control techniques, has been proposed. Many works recommend the combination of SM with PD control [35–37, 39–41]. As a result, the achievements are chattering reduction, shorter settling time, smoother control input [35, 37] and model free approach [39–41]. Alternatively, Truong et al. [38] propose the combination of SM with a neural network in order to achieve higher tracking performance. Lin and Wai [42] studied the combination of the Computed Torque control and the fuzzy neural network in a 1-dof planar mechanism. On the other hand, the hybridization of the Computed Torque and Sliding Mode controls was investigated by Yu [43] and Peng et al. [44] in 2-dof planar mechanisms. Furthermore, most of the published papers show only simulations, see for example refs. [18–20, 23, 35, 36, 39–41, 43–47] and few experimental result. [33, 37, 38, 42, 48–50]

1.2. Objectives

This paper presents a comparison of the performance of hybrid control techniques with the pure ones in parallel robots. Basically, the authors propose the combination of a modified Sliding Mode technique with other conventional ones, namely, the PD and the Computed Torque controls. In order to validate the theoretical predictions and evaluate their behaviour in terms of the end-effector path control in transient and steady states, experimental tests in a planar parallel robot are conducted. Moreover, simulations are also conducted to evaluate the behaviour of a 3-dof spatial parallel robot, when performing a 3D-path. The evaluation of the performance is done by computing the root-mean-square values of the path tracking error and actuator torques during the entire motion cycle.

1.3. About the paper sections

Section 2 deals with the theoretical foundations for the combination of distinct control techniques, while Section 3 presents a detailed description of the experimental setup and the obtained experimental results. Section 4 treats the performance of the hybrid controls from a conducted simulation of a spatial parallel robot. Finally, Section 5 addresses a discussion, and the main conclusions are drawn in Section 6.

https://doi.org/10.1017/S0263574721000874 Published online by Cambridge University Press

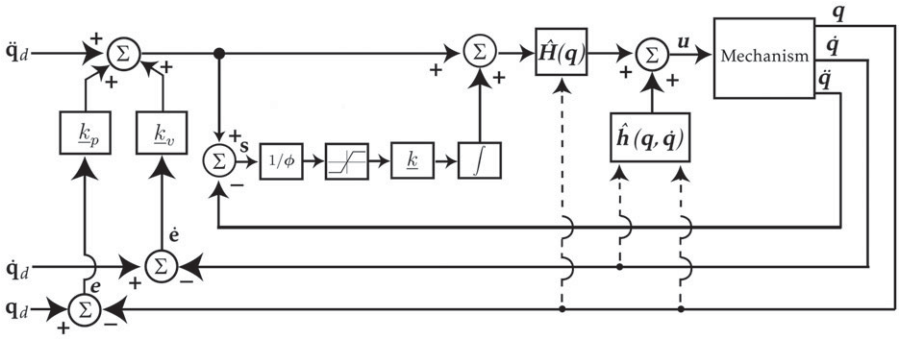


Figure 1. *Block diagram of the proposed hybrid controls.*

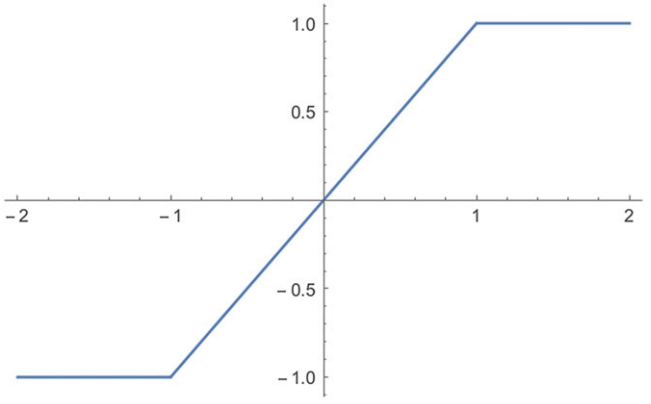


Figure 2. *Plot of the function sat(x).*

2. Proposed Hybrid Control Law and Stability Analysis

The dynamic model of a mechanical system can be described by the following equation [13, 51]

$$\mathbf{H}(\boldsymbol{q})\,\ddot{\boldsymbol{q}} + \boldsymbol{h}(\boldsymbol{q}, \dot{\boldsymbol{q}}) = \boldsymbol{u} \tag{1}$$

where $\boldsymbol{q}$ is the vector of the generalized and independent coordinates, $\mathbf{H}(\boldsymbol{q})$ is the inertia matrix, $\boldsymbol{h}(\boldsymbol{q}, \dot{\boldsymbol{q}})$ is the vector of the centrifugal, Coriolis, gravitational and friction terms, while $\boldsymbol{u}$ is the control effort. Here, the control law for the proposed hybrid controls (Figure 1) is given by

$$\boldsymbol{u} = \hat{\mathbf{H}}(\boldsymbol{q}) \left(\ddot{\boldsymbol{q}}_d + \underline{k}_v\, \dot{\boldsymbol{e}} + \underline{k}_p\, \boldsymbol{e} + \int_0^t \underline{k}\, \mathrm{sat}(\boldsymbol{s}/\boldsymbol{\phi})\, d\tau \right) + \hat{\boldsymbol{h}}(\boldsymbol{q}, \dot{\boldsymbol{q}}) \tag{2}$$

where $\boldsymbol{q}_d$ is the reference signal, $\boldsymbol{e}$ is the error signal, defined by $\boldsymbol{e} = \boldsymbol{q}_d - \boldsymbol{q}$, $\hat{\mathbf{H}}(\boldsymbol{q})$ and $\hat{\boldsymbol{h}}(\boldsymbol{q}, \dot{\boldsymbol{q}})$ are estimations of $\mathbf{H}(\boldsymbol{q})$ and $\boldsymbol{h}(\boldsymbol{q}, \dot{\boldsymbol{q}})$, respectively, and $\underline{k}_v$, $\underline{k}_p$ and $\underline{k}$ are positive definite diagonal matrices. Additionally, the variable $\boldsymbol{s}$ is defined as

$$\boldsymbol{s} = \ddot{\boldsymbol{e}} + \underline{k}_v\, \dot{\boldsymbol{e}} + \underline{k}_p\, \boldsymbol{e} \tag{3}$$

The vector division used in the expression $\mathrm{sat}(\boldsymbol{s}/\boldsymbol{\phi})$ is defined as the division term by term, while Eq. (4) defines the saturation function (Figure 2)

$$\mathrm{sat}(x) = \begin{cases} x, & |x| < 1 \\ \mathrm{sgn}(x), & |x| \geq 1 \end{cases} \tag{4}$$

https://doi.org/10.1017/S0263574721000874 Published online by Cambridge University Press

The parameter vector $\boldsymbol{\phi}$ means the thickness of the boundary layer defined in a small vicinity with respect to the sliding surface. The purpose of the saturation function is to smooth the control discontinuity of the signum function and reduce chattering. [37, 39, 41, 52] Note that for $\underline{k} = \boldsymbol{0}$, the control law becomes the Computed Torque control law. Since the term $\int_0^t \underline{k}\,\mathrm{sat}(\boldsymbol{s}/\boldsymbol{\phi})\,d\tau$ comes from the Sliding Mode control [25, 27, 35], the control law can be considered hybrid.

2.1. Stability analysis

Theorem 1.(refs. [53, 54]) Consider a non-linear system $\dot{\mathbf{x}}(t) = \boldsymbol{f}(\mathbf{x}, t)$, where $\mathbf{x} \in \mathbb{R}^n$, $\mathbf{x}(0) = \mathbf{x}_0$ is the initial state, and the origin $\mathbf{x} = \mathbf{0}$ is the equilibrium point. Suppose there are two real numbers $\rho > 0$, $0 < \beta < 1$, and a continuously differentiable positive function $V{:}\mathbb{R}^n \to \mathbb{R}$, such that the inequality

$$\dot{V}(\mathbf{x}) + \rho V(\mathbf{x})^{\beta} \leq 0 \tag{5}$$

is always fulfilled for any solution $\mathbf{x}(t, \mathbf{x}_0)$ of the system. Then, the equilibrium point is globally finite-time stable. In addition, the settling time t_s, which depends on the initial state, satisfies the following inequality

$$t_s \leq \frac{1}{(1-\beta)\,\rho}\, V(\mathbf{x}_0)^{1-\beta} = t^*$$

Proof. Assuming that $\mathbf{x} \neq \mathbf{0}$, inequality (5) can be divided by V^{β},

$$V^{-\beta}\frac{dV}{dt} + \rho \leq 0 \tag{6}$$

Integrating (6) with respect to time from 0 to t,

$$\int_{V(\mathbf{x}_0)}^{V(\mathbf{x})} V^{-\beta} dV + \int_0^t \rho\, d\tau \leq 0$$

$$\frac{V^{1-\beta}}{1-\beta}\bigg|_{V(\mathbf{x}_0)}^{V(\mathbf{x})} + \rho\,(t-0) \leq 0$$

$$V(\mathbf{x})^{1-\beta} \leq V(\mathbf{x}_0)^{1-\beta} - (1-\beta)\,\rho\, t \tag{7}$$

Notice that the right side of inequality (7), which corresponds to the upper bound of $V(\mathbf{x})^{1-\beta}$, decreases linearly as t increases its value and becomes negative for $t > t^*$. On the other hand, by definition, since $V(\mathbf{x})$ is continuous and positive, the lower bound of $V(\mathbf{x})^{1-\beta}$ is zero. Considering that inequality (7) is only valid for $\mathbf{x} \neq 0$; hence, $V(\mathbf{x})^{1-\beta}$ converges to zero and, consequently, V as well, in a finite time lesser or equal t^* and, therefore, the system is globally finite-time stable.

Replacing the control effort $\boldsymbol{u}$ (Eq. (2)) in Eq. (1) and subtracting $\hat{\mathbf{H}}\,\ddot{\boldsymbol{q}} + \hat{\boldsymbol{h}}$ in both sides,

$$\mathbf{H}\,\ddot{\boldsymbol{q}} + \boldsymbol{h} - \hat{\mathbf{H}}\,\ddot{\boldsymbol{q}} - \hat{\boldsymbol{h}} = \hat{\mathbf{H}}\left(\ddot{\boldsymbol{q}}_d + \underline{k}_v\dot{\boldsymbol{e}} + \underline{k}_p\boldsymbol{e} + \int_0^t \underline{k}\,\mathrm{sat}(\boldsymbol{s}/\boldsymbol{\phi})\,d\tau\right) + \hat{\boldsymbol{h}} - \hat{\mathbf{H}}\,\ddot{\boldsymbol{q}} - \hat{\boldsymbol{h}} \tag{8}$$

Since $\boldsymbol{e} = \boldsymbol{q}_d - \boldsymbol{q}$, and defining $\tilde{\mathbf{H}} = \mathbf{H} - \hat{\mathbf{H}}$ and $\tilde{\boldsymbol{h}} = \boldsymbol{h} - \hat{\boldsymbol{h}}$

$$\tilde{\mathbf{H}}\,\ddot{\boldsymbol{q}} + \tilde{\boldsymbol{h}} = \hat{\mathbf{H}}\left(\ddot{\boldsymbol{e}} + \underline{k}_v\dot{\boldsymbol{e}} + \underline{k}_p\boldsymbol{e} + \int_0^t \underline{k}\,\mathrm{sat}(\boldsymbol{s}/\boldsymbol{\phi})\,d\tau\right) \tag{9}$$

Hence,

$$\tilde{\mathbf{H}}\,\ddot{\boldsymbol{q}} + \tilde{\boldsymbol{h}} = \hat{\mathbf{H}}\left(\boldsymbol{s} + \int_0^t \underline{k}\,\mathrm{sat}(\boldsymbol{s}/\boldsymbol{\phi})\,d\tau\right) \tag{10}$$

https://doi.org/10.1017/S0263574721000874 Published online by Cambridge University Press

Multiplying both sides from the left by $\hat{\mathbf{H}}^{-1}$, the following expression is obtained

$$\boldsymbol{s} + \int_0^t \underline{k}\, \text{sat}(\boldsymbol{s}/\boldsymbol{\phi})\, d\tau = \boldsymbol{\epsilon} \tag{11}$$

where

$$\boldsymbol{\epsilon} = \hat{\mathbf{H}}^{-1}(\tilde{\mathbf{H}}\,\ddot{\boldsymbol{q}} + \tilde{\boldsymbol{h}}) \tag{12}$$

In addition, differentiating Eq. (11) with respect to time

$$\dot{\boldsymbol{s}} + \underline{k}\, \text{sat}(\boldsymbol{s}/\boldsymbol{\phi}) = \dot{\boldsymbol{\epsilon}} \tag{13}$$

Since $\underline{k}$ is a diagonal matrix, there is no coupling between the components of $\boldsymbol{s}$ and the dynamics of each component of $\boldsymbol{s}$ can be written as

$$\dot{s}_i + k_i\, \text{sat}(s_i/\phi_i) = \dot{\epsilon}_i \tag{14}$$

Furthermore, consider the Lyapunov candidate function $V_i(s_i)$, expressed as

$$V_i(s_i) = \frac{1}{2}\, s_i^2 \geq 0 \tag{15}$$

Differentiating $V_i(s_i)$ with respect to time

$$\frac{\mathrm{d}}{\mathrm{d}t}\big(V_i(s_i)\big) = s_i \dot{s}_i \tag{16}$$

Isolating $\dot{s}_i$ in Eq. (14) and replacing it in the previous equation

$$\dot{V}_i = s_i\, (\dot{\epsilon}_i - k_i\, \text{sat}(s_i/\phi_i)) \tag{17}$$

In addition, s_i and $\text{sat}(s_i/\phi_i)$ can be replaced by $|s_i|\ \text{sgn}(s_i)$ and $\text{sat}(|s_i|/\phi_i))\ \text{sgn}(s_i)$, respectively,

$$\begin{aligned} \dot{V}_i &= |s_i|\ \text{sgn}(s_i)\, (\dot{\epsilon}_i - k_i\, \text{sat}(|s_i|/\phi_i)\text{sgn}(s_i)) \\ &= |s_i|\, (\dot{\epsilon}_i\, \text{sgn}(s_i) - k_i\, \text{sat}(|s_i|/\phi_i)) \end{aligned} \tag{18}$$

Assuming there are no modelling errors, then

$$\boldsymbol{\epsilon} = \boldsymbol{0} \Rightarrow \dot{\boldsymbol{\epsilon}} = \boldsymbol{0} \tag{19}$$

$$\therefore \dot{V}_i(s_i) = -k_i\, |s_i|\ \text{sat}(|s_i|/\phi_i) < 0,\ s_i \neq 0 \tag{20}$$

Even though this assumption is not very realistic, it is commonly used in the proof of stability of control laws, like the Computed Torque Control. On the other hand, when there are modelling errors ($\boldsymbol{\epsilon} \neq \boldsymbol{0}$), some further analysis can be conducted. Assuming that the system is outside the boundary layer, which means that $|s_i| \geq \phi_i$ Eq. (18) can be written as

$$\begin{aligned} \dot{V}_i(s_i) &= |s_i|\, (\dot{\epsilon}_i \text{sgn}(s_i) - k_i) \\ &\leq |s_i|\, (|\dot{\epsilon}_i| - k_i) \end{aligned} \tag{21}$$

Additionally, since $\dot{\epsilon}_i$ is bounded (assuming the system never assume configurations where $\hat{\mathbf{H}}$ is singular), it is possible to select a positive number δ_i [52–54] that satisfies the condition $|\dot{\epsilon}_i| \leq \delta_i$. Hence, choosing a value for k_i such that $k_i > \delta_i$:

$$\dot{V}_i \leq |s_i|\, (|\dot{\epsilon}_i| - k_i) \leq |s_i|\, (\delta_i - k_i) \leq 0$$

https://doi.org/10.1017/S0263574721000874 Published online by Cambridge University Press

Also, note that $|s_i|$ equals to $\sqrt{2V_i}$. Hence,

$$\dot{V}_i \leq -\sqrt{2V_i}\,(k_i - \delta_i) \leq -\sqrt{2}\,(k_i - \delta_i)\,V_i^{1/2}$$
$$\therefore \dot{V}_i + \sqrt{2}\,(k_i - \delta_i)\,V_i^{1/2} \leq 0 \tag{22}$$

Notice that inequality (22) falls into the same category of inequality (5) of Theorem 1, where $\rho = \sqrt{2}\,(k_i - \delta_i) > 0$ and $\beta = 1/2$. Therefore, in the limit case where there is no boundary layer ($\phi_i \to 0$ and $\text{sat}(s_i/\phi_i) \to \text{sgn}(s_i)$), the proposed hybrid control law makes the equilibrium point $s_i = 0$ globally finite-time stable. Also, after reaching the sliding surface $s_i = 0$, the error signal e_i will decrease exponentially to zero, since $s_i = \ddot{e}_i + k_{v_i}\dot{e}_i + k_{p_i}e_i$. In this limit case, the reaching time to the sliding surface satisfies the following inequality,

$$t_{s\,i} \leq \frac{\sqrt{2}}{(k_i - \delta_i)}\,V_i\,(s_i(0))^{1/2} = t_i^*$$

Additionally, for an arbitrary value of ϕ_i, one can affirm that the variable s_i will reach the boundary layer $|s_i| \leq \phi_i$ in a finite time equals or lesser than t_i^* and, consequently, $|e_i|$ will also be bounded for $t \geq t_i^*$. According to the theory of linear control [13, 51], the damping ratio of the second-order system $\ddot{e}_i + k_{v_i}\dot{e}_i + k_{p_i}e_i = s_i$ is given by $\zeta = \frac{k_{v_i}}{2\sqrt{k_{p_i}}}$. Since there is no overshoot nor resonance for $\zeta \geq 1$ and the DC gain of the system is $1/k_{p_i}$, one can conclude that for $k_{v_i} \geq 2\sqrt{k_{p_i}}$, the upper bound of $|e_i|$ becomes ϕ_i/k_{p_i}.

3. Experiments

The experimental tests focus on applying hybrid control techniques to a parallel robot. The chosen parallel robot has three subsystems, namely, mechanical, actuation and control. Regarding the mechanical subsystem, it is composed of a 2-dof planar parallel mechanism [39, 40, 49], commonly known as 5R mechanism (Fig. 3(a)), which has four moving links and one fixed one, all connected by revolute joints. The dimensional parameters are the lengths $l_0, l_1, l_2, l_{i_{g_1}}, l_{i_{g_2}}$, while the inertial parameters are the masses m_{i1}, m_{i2}, and the mass moments of inertia $J_{i_{z_1}}, J_{i_{z_2}}$ with respect to the centre of mass of each moving link that belongs to the kinematic chain S_i (Fig. 3). Additionally, b_i and μ_i are, respectively, the viscous and dry friction coefficients at the actuated revolute joints.

3.1. Control strategies

For comparison purposes, the following control laws have been defined for use in the experiment, all in the joint space:

- Proportional Derivative with acceleration feed-forward (PD)

$$\boldsymbol{u} = \underline{m}^*(\ddot{\boldsymbol{q}}_d + \underline{k}_v\dot{\boldsymbol{e}} + \underline{k}_p\boldsymbol{e}) \tag{23}$$

- Proportional Derivative with acceleration feed-forward + Sliding Mode (PD+SM)

$$\boldsymbol{u} = \underline{m}^*\left(\ddot{\boldsymbol{q}}_d + \underline{k}_v\dot{\boldsymbol{e}} + \underline{k}_p\boldsymbol{e} + \int_0^t \underline{k}\,\text{sat}(\boldsymbol{s}/\boldsymbol{\phi})\text{d}\tau\right) \tag{24}$$

- Computed Torque (CT)

$$\boldsymbol{u} = \hat{\mathbf{H}}(\boldsymbol{q})\,(\ddot{\boldsymbol{q}}_d + \underline{k}_v\dot{\boldsymbol{e}} + \underline{k}_p\boldsymbol{e}) + \hat{\boldsymbol{h}}(\boldsymbol{q}, \dot{\boldsymbol{q}}) \tag{25}$$

- Computed Torque + Sliding Mode (CT+SM)

$$\boldsymbol{u} = \hat{\mathbf{H}}(\boldsymbol{q})\left(\ddot{\boldsymbol{q}}_d + \underline{k}_v\dot{\boldsymbol{e}} + \underline{k}_p\boldsymbol{e} + \int_0^t \underline{k}\,\text{sat}(\boldsymbol{s}/\boldsymbol{\phi})\text{d}\tau\right) + \hat{\boldsymbol{h}}(\boldsymbol{q}, \dot{\boldsymbol{q}}) \tag{26}$$

https://doi.org/10.1017/S0263574721000874 Published online by Cambridge University Press

Table I. *Dimensional and inertial parameters of the chains S_i of the mechanism.*

S_1	ℓ_0 (m)	ℓ_1 (m)	ℓ_2 (m)	ℓ_{1g_1} (m)	ℓ_{1g_2} (m)	
	0.05	0.12	0.16	0.06	0.078	
	m_{11} (kg)	m_{12} (kg)	J_{1z_1} (kgm^2)	J_{1z_2} (kgm^2)	b_1 (Nm s)	μ_1 (Nm)
	0.062	0.124	2.542×10^{-4}	5.769×10^{-4}	1.226×10^{-4}	4.457×10^{-2}
S_2	ℓ_0 (m)	ℓ_1 (m)	ℓ_2 (m)	ℓ_{2g_1} (m)	ℓ_{2g_2} (m)	
	0.05	0.12	0.16	0.06	0.058	
	m_{21} (kg)	m_{22} (kg)	J_{2z_1} (kgm^2)	J_{2z_2} (kgm^2)	b_2 (Nm s)	μ_2 (Nm)
	0.062	0.097	2.960×10^{-4}	3.307×10^{-4}	2.039×10^{-4}	4.992×10^{-2}

Table II. *Controller parameters for the circular path.*

Technique	λ (rad/s)	m^* (kg m^2)	ϕ (rad/s^2)	k (rad/s^2)
PD	35	3.58×10^{-3}	–	–
PD+SM	35	3.58×10^{-3}	20	200
CT	60	–	–	–
CT+SM	60	–	20	363

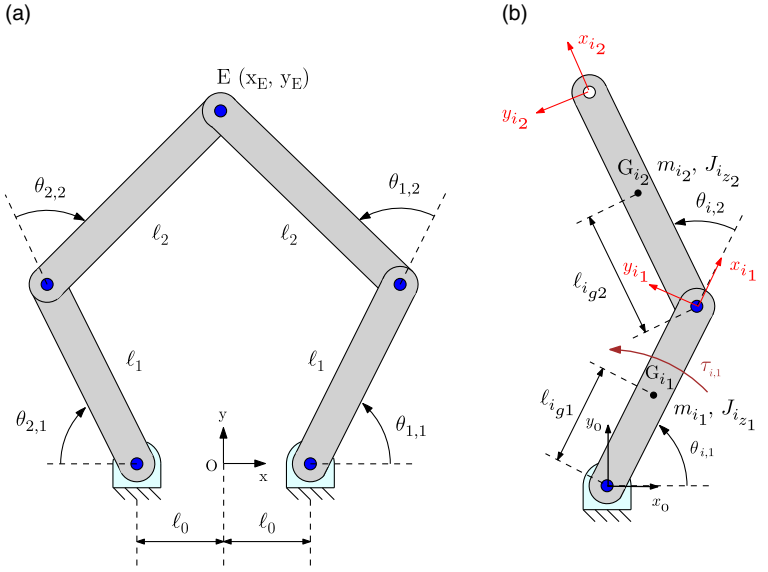


Figure 3. *(a) 5R parallel mechanism; (b) a RR kinematic chain S_i.*

For the PD and PD+SM controls, the constant diagonal matrix $\underline{m}^*$ replaces the inertia matrix $\hat{\mathbf{H}}$. The elements of $\underline{m}^*$ are obtained from the elements of the diagonal of $\hat{\mathbf{H}}$ at a central configuration with respect to the robot workspace and are available in Table II. Additionally, for both controls, the term $\hat{\boldsymbol{h}} = \boldsymbol{0}$. In the CT+SM control law, the full dynamic model presented in Appendix A is used to calculate the estimations of $\hat{\mathbf{H}}$ and $\hat{\boldsymbol{h}}$. Note that CT and PD control laws can be generated by making $\underline{k} = 0$ in CT+SM and PD+SM laws, respectively. Figure 4 shows the block diagram of the overall control loop in the joint space.

In order to estimate, for instance, the angular velocities of the actuator shafts from the angular displacement measurements provided by the encoders, the numerical differentiation is implemented by applying the finite difference method. Aiming to avoid the amplification of high-frequency noise of the

https://doi.org/10.1017/S0263574721000874 Published online by Cambridge University Press

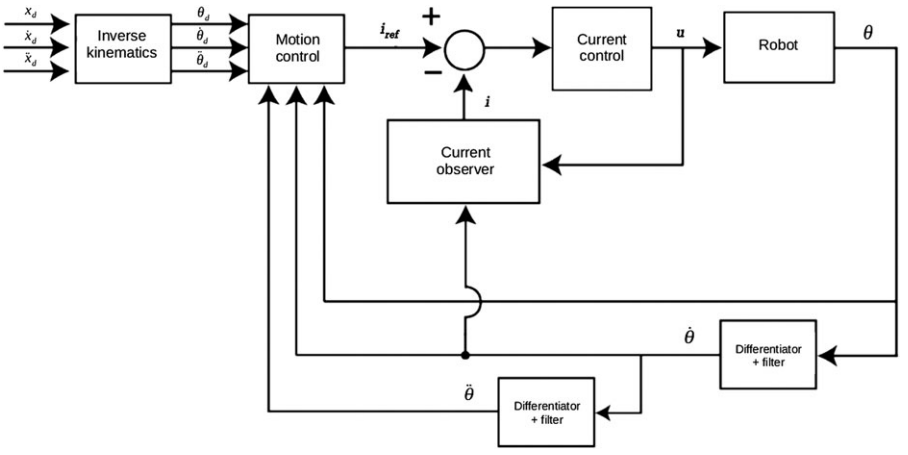


Figure 4. *The block diagram of the overall control loop in the joint space.*

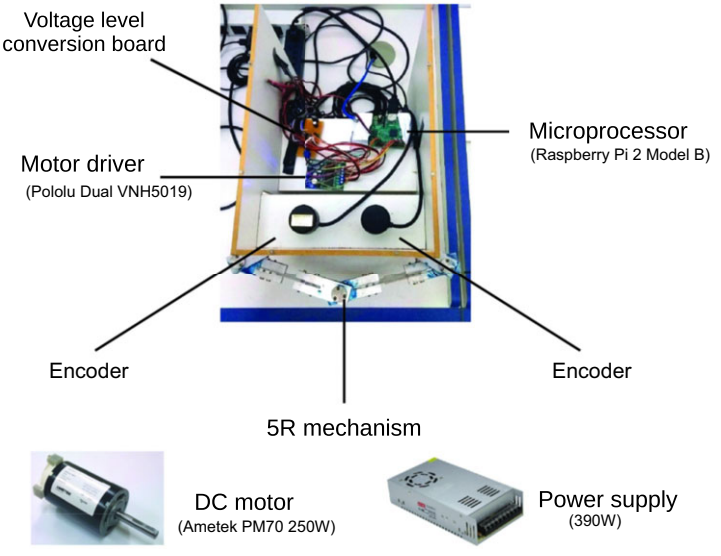


Figure 5. *The components of the robot systems.*

acquired signal due to the use of finite difference technique, the numerical differentiations are employed in series with two types of filters. For the velocity estimation from the position measurements, a second-order Bessel low-pass filter is used, while for the acceleration estimation from the velocity computation, an eight-order Bessel low-pass filter is employed [55].

3.2. Experimental test-bed

Figure 5 shows the components of the robot systems. Constructively, the mechanical system (Fig. 6) has five revolute joints which correspond to rigid ball bearings. For the moving links, flat bars made of aluminium alloy and acrylic are employed. In addition, once the motion plane is horizontal, the dynamic model does not take into account the gravitational forces [49].

Regarding the actuation system, it is composed of two direct drive DC motors (250 W each) AMETEK PM70, one motor driver Pololu Dual VNH5019, and a switched-mode power supply (24V, 390 W).

https://doi.org/10.1017/S0263574721000874 Published online by Cambridge University Press

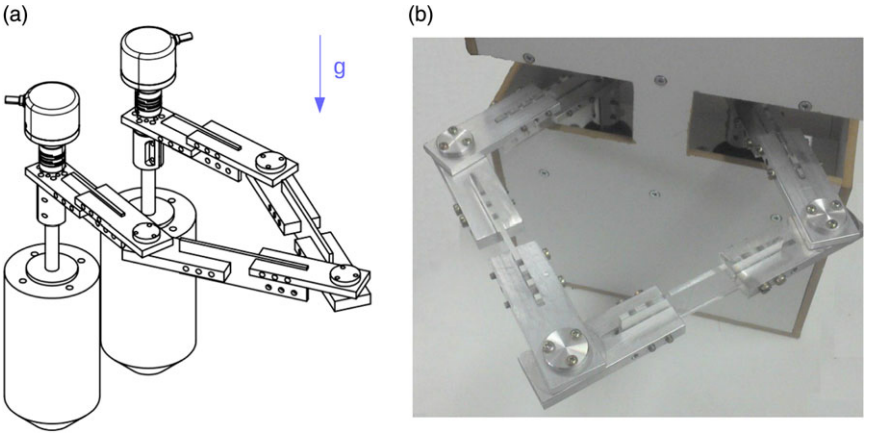


Figure 6. *The mechanical system: (a) CAD model; (b) 5R mechanism.*

The control system has two incremental rotary encoders E40S (5000 quad-counts per turn) and one microprocessor Raspberry Pi 2 model B. Additionally, there is an electronic circuit board for the conversions of the voltage levels, from the power supply to the encoder (24–15V), and from the encoders to the microprocessor (0–15V to 0–3.3V).

3.3. Paths

The centre coordinates (0;158 mm) and the radius 50 mm define the circular path, which the end-effector performs it clockwise with constant tangential velocity. Additionally, the duration of one cycle of the path is 1 s. In each test, the total acquisition time for measuring the experimental data comprises 8 cycles. After the 8 cycles, the reference signal is fixed in its last position, forcing a sudden stop.

The triangular path is defined by three vertices, which are (−2 mm;108 mm), (50 mm;258 mm) and (−50 mm;258 mm) and is performed counterclockwise. Moreover, the end-effector takes 0.75 s to go from one vertex to the other, whose kinematic variables are interpolated by a seventh-order polynomial. Regarding the conditions to determinate the polynomial coefficients, they are the initial and final coordinates of the end-effector. Moreover, the velocities, accelerations and jerks are all null at the vertices of each side of the triangular path. In each test, the total acquisition time for measuring the experimental data comprises 2 cycles. Additionally, in both paths, the end-effector starts from the position (−2 mm;108 mm).

3.4. Controller gains

In order to impose the same dynamics in both components of the control error and critical damping at the closed-loop system poles, the matrices $\underline{k}_p$, $\underline{k}_v$, $\underline{k}$, $\underline{m}^*$ and the vector $\boldsymbol{\phi}$ are parametrized as follows,

$$\underline{k}_p = \lambda^2 \mathbf{1} \tag{27}$$

$$\underline{k}_v = 2\lambda \mathbf{1} \tag{28}$$

$$\underline{k} = k\mathbf{1} \tag{29}$$

$$\underline{m}^* = m^* \mathbf{1} \tag{30}$$

$$\boldsymbol{\phi} = \phi \begin{bmatrix} 1 & 1 \end{bmatrix}^T \tag{31}$$

where $\mathbf{1}$ is the identity matrix.

https://doi.org/10.1017/S0263574721000874 Published online by Cambridge University Press

Table III. *Controller parameters for the triangular path.*

Technique	λ (rad/s)	m^* (kg m^2)	ϕ (rad/s^2)	k (rad/s^2)
PD	25	3.58×10^{-3}	–	–
PD+SM	25	3.58×10^{-3}	90	200
CT	60	–	–	–
CT+SM	60	–	20	363

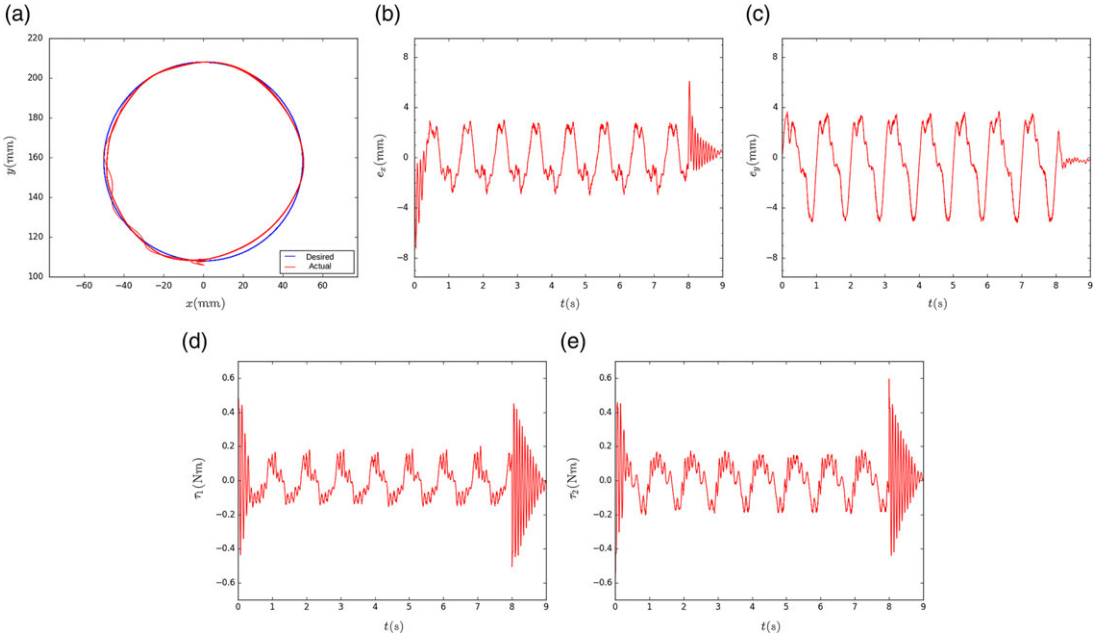


Figure 7. *Pure PD control: circular path. (a) Desired and actual circular paths. (b) x-direction control error. (c) y-direction control error. (d) Torque of actuator 1. (e) Torque of actuator 2.*

The controller parameters for each technique and prescribed path are shown in Tables II and III. The parameter λ corresponds to the desired natural frequency of the closed-loop system poles.

3.5. Experimental results

The experimental results comprise a comparison between the desired and actual paths, the path tracking errors in the *x*- and *y*-directions, and the actuator torques. For the circular path, the plots for the PD, PD+SM, CT and CT+SM are shown in Figs. 7, 8, 9 and 10, respectively. For the triangular path, the plots for the PD, PD+SM, CT and CT+SM are shown in Figs. 11, 12, 13 and 14, respectively.

Tables IV and V show the metrics for the circular and triangular paths, respectively. In the second column of these tables, the term *error* means the root-mean-square value of the path tracking error of the defined path during the entire motion cycle. Similarly, in the fourth column, the term *torque* means the root-mean-square value of a composition of the actuator torques related to the path during the correspondent cycle. Regarding the term *difference*, that appears in the third and fifth columns of Tables IV and V, it means the relative percent difference between the considered metrics values of the pure control and the hybrid control, assuming the pure control as the reference value.

From those tables, one can observe that the hybrid controls cause a reduction of the path tracking error in both paths. On the other hand, the hybrid controls are responsible for the increase of the actuator torques in the analysed paths. Additionally, a model-based hybrid control shows better results for the

https://doi.org/10.1017/S0263574721000874 Published online by Cambridge University Press

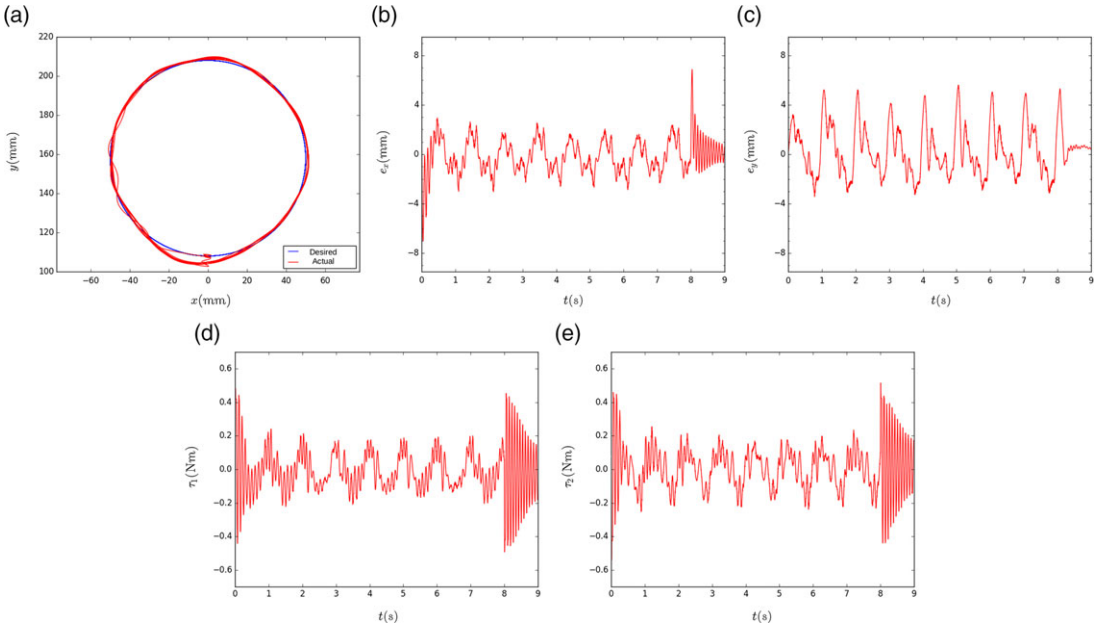


Figure 8. *Hybrid PD+SM control: circular path. (a) Desired and actual circular paths. (b) x-direction control error. (c) y-direction control error. (d) Torque of actuator 1. (e) Torque of actuator 2.*

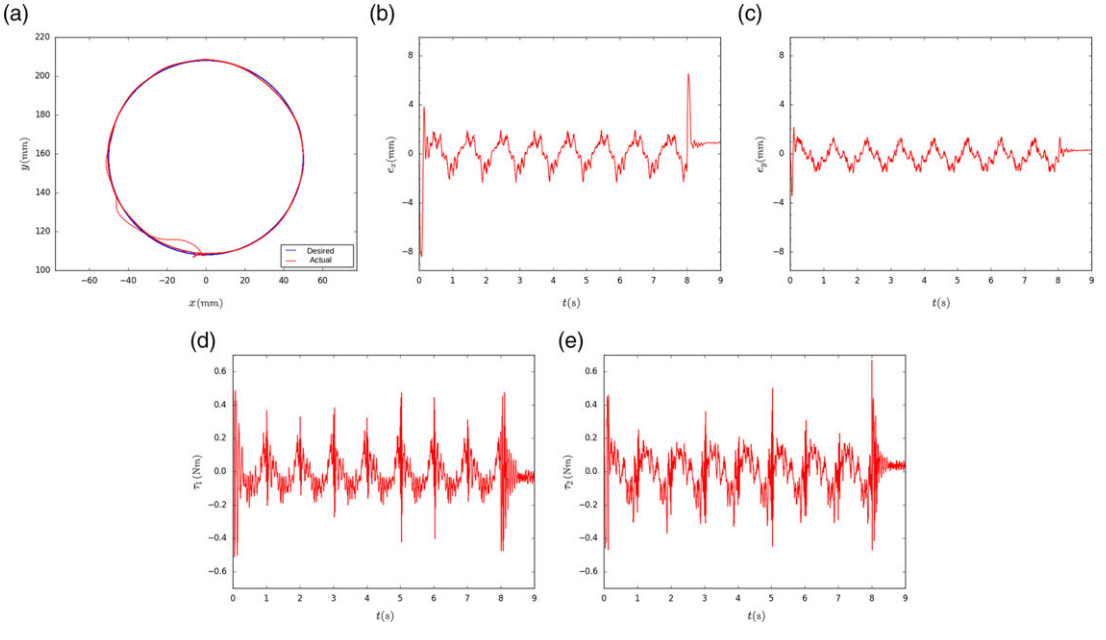


Figure 9. *Pure CT control: circular path. (a) Desired and actual circular paths. (b) x-direction control error. (c) y-direction control error. (d) Torque of actuator 1. (e) Torque of actuator 2.*

path tracking error than a hybrid control that is not based on a model. For the triangular path, not only the model-based hybrid control improves the performance of the robot in terms of the path tracking error but also with respect to the actuator torques, in a comparison with the non-model-based one.

Table VI presents the steady-state error for the two analysed paths. The CT+SM is the control technique that has the best performance with lower errors in both paths. Despite the fact that the Computed

https://doi.org/10.1017/S0263574721000874 Published online by Cambridge University Press

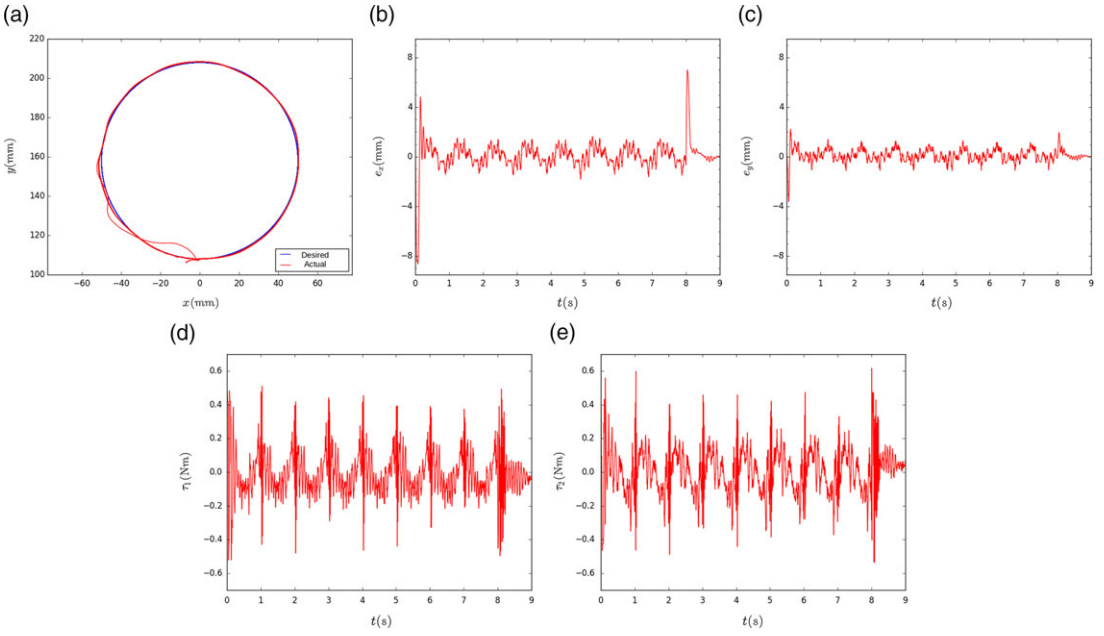


Figure 10. *Hybrid CT+SM control: circular path. (a) Desired and actual circular paths. (b) x-direction control error. (c) y-direction control error. (d) Torque of actuator 1. (e) Torque of actuator 2.*

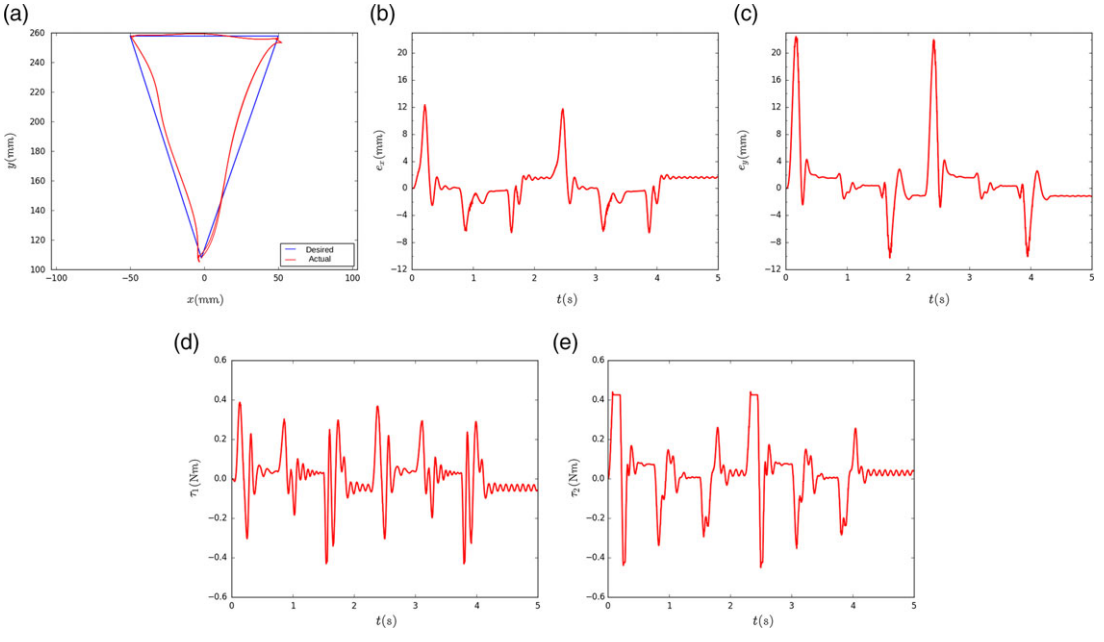


Figure 11. *Pure PD control: triangular path. (a) Desired and actual circular paths. (b) x-direction control error. (c) y-direction control error. (d) Torque of actuator 1. (e) Torque of actuator 2.*

Torque control does not demonstrate a good steady-state error performance in the circular path, for the triangular path, the CT control shows lower error values in comparison with the PD and PD+SM controls.

https://doi.org/10.1017/S0263574721000874 Published online by Cambridge University Press

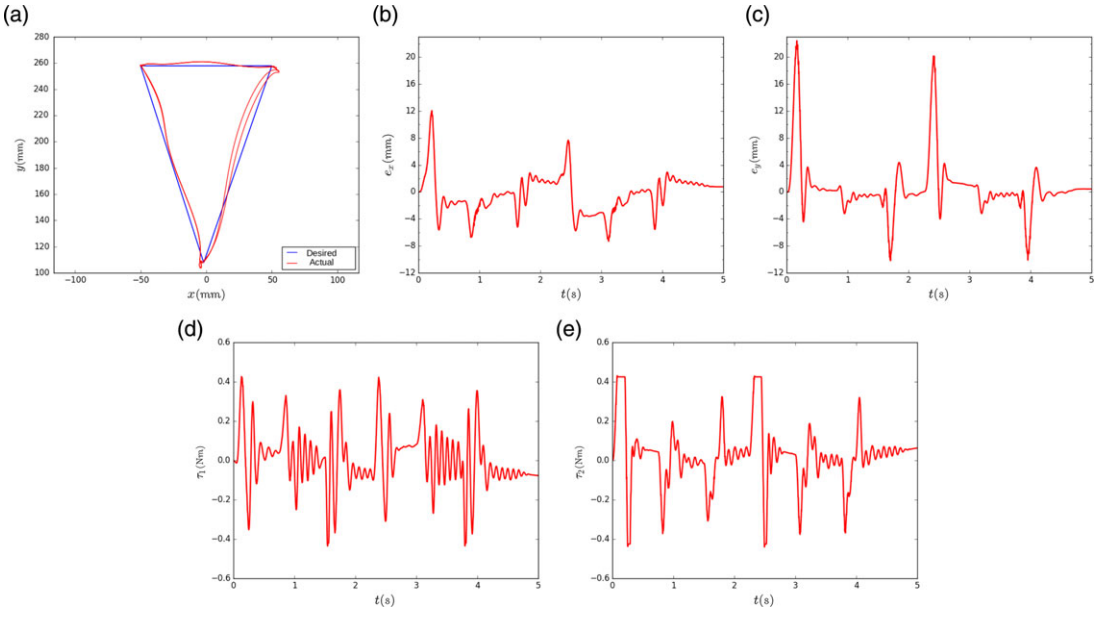


Figure 12. *Hybrid PD+SM control: triangular path. (a) Desired and actual circular paths. (b) x-direction control error. (c) y-direction control error. (d) Torque of actuator 1. (e) Torque of actuator 2.*

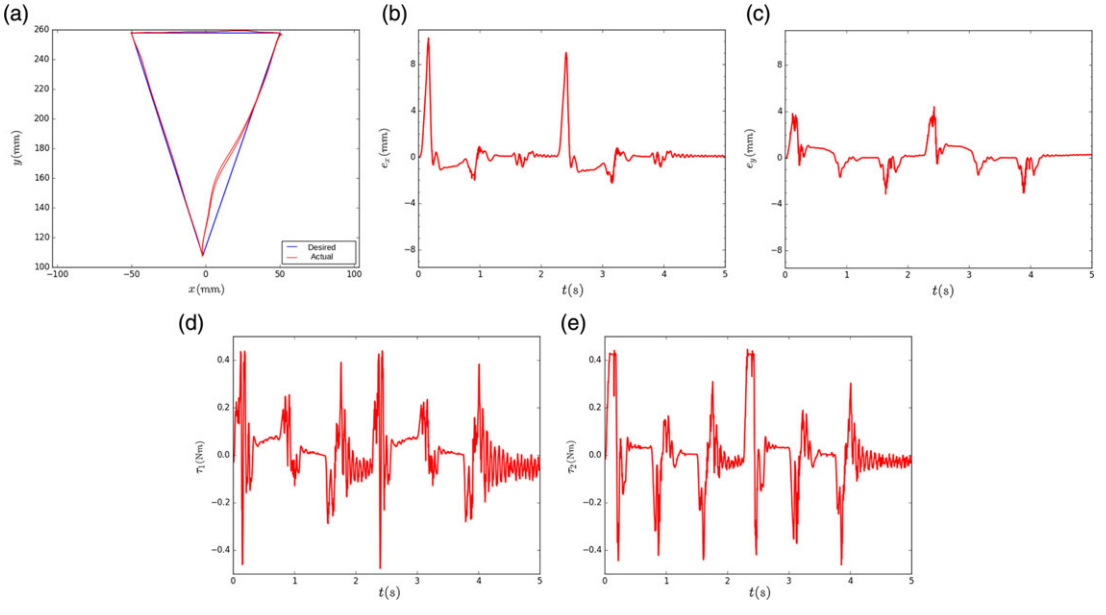


Figure 13. *Pure CT control: triangular path. (a) Desired and actual circular paths. (b) x-direction control error. (c) y-direction control error. (d) Torque of actuator 1. (e) Torque of actuator 2.*

4. Simulations

In order to evaluate the effectiveness of the proposed hybrid controls in a spatial parallel robot, the 2RRRS+P(Pa)P is selected as the mechanical structure. It consists of a topologically asymmetric parallel robot whose end-effector is able to perform three linear and independent displacements. The robot has three active kinematic chains, two of them are identical RRRS, while the other remaining is P(Pa)P.

https://doi.org/10.1017/S0263574721000874 Published online by Cambridge University Press

Table IV. *Metrics for the circular path.*

Control	Error (mm)	Difference (%)	Torque (Nm)	Difference (%)
PD	3.15	–	0.132	–
PD+SM	2.37	−24.8	0.141	+ 6.81
CT	1.14	–	0.143	–
CT+SM	0.77	−32.4	0.168	+ 17.5

Table V. *Metrics for the triangular path.*

Control	Error (mm)	Difference (%)	Torque (Nm)	Difference (%)
PD	5.39	–	0.197	–
PD+SM	5.16	−4.27	0.212	+ 7.61
CT	1.85	–	0.181	–
CT+SM	1.63	−11.9	0.191	+ 5.52

Table VI. *Steady-state error (mm) for the two paths.*

Control	Circular path	Triangular path
PD	0.484	1.972
PD+SM	0.494	0.874
CT	0.949	0.279
CT+SM	0.041	0.033

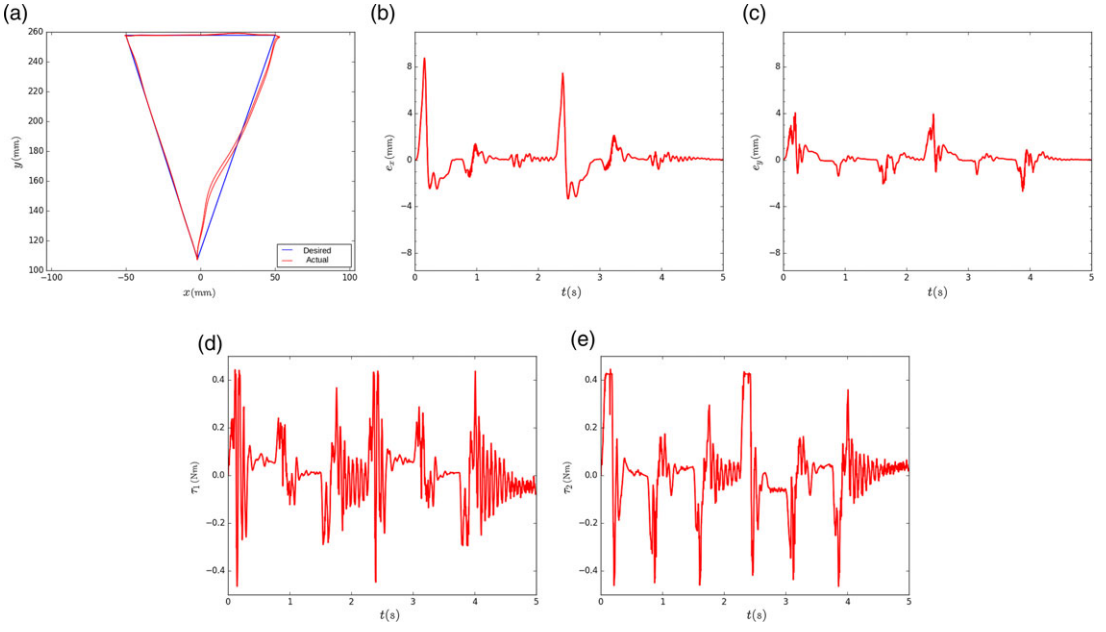


Figure 14. *Hybrid CT+SM control: triangular path. (a) Desired and actual circular paths. (b) x-direction control error. (c) y-direction control error. (d) Torque of actuator 1. (e) Torque of actuator 2.*

https://doi.org/10.1017/S0263574721000874 Published online by Cambridge University Press

Table VII. *Controller parameters for the chosen path.*

Technique	λ **(rad/s)**	$\underline{m}^*$ **(kg)**	ϕ **(m/s^2)**	k **(m/s^2)**
PD	60	diag(0.88, 0.45, 0.87)	–	–
PD+SM	60	diag(0.88, 0.45, 0.87)	40	500
CT	60	–	–	–
CT+SM	60	–	40	500

Table VIII. *Metrics for the chosen path.*

Control	**Error (mm)**	**Difference (%)**	**Torque**[a] **(Nm)**	**Difference (%)**
PD	13.195	–	2.865	–
PD+SM	1.212	−90.8	2.972	+3.76
CT	0.961	–	2.970	–
CT+SM	0.852	−11.3	2.970	−0.026

[a]For the actuator 3, the torque is computed by assuming a pulley-timing belt transmission, with a pitch radius of 25 mm.

Table IX. *Steady-state error (mm) for the chosen path.*

Control	**Chosen path**
PD	13.941
PD+SM	0.012
CT	0.400
CT+SM	0.009

The letters R, P, S and Pa of the literal notation stand for revolute, prismatic, spherical and parallelogram joints, respectively. Particularly, the underlined ones correspond to the active joints. In Appendix B, Fig. B.1 shows the mechanism structure diagram, the employed variables, the parameters, the centres of mass and the actuator torques and force. In addition, the reader can also find in Table B.1 the selected parameters for the simulations. Furthermore, the full dynamic model is available in ref. [57]. Regarding the chosen path, the coordinates of the end-effector with respect to time are defined as follows,

$$\begin{bmatrix} x_E(t) \\ y_E(t) \\ z_E(t) \end{bmatrix} = \begin{bmatrix} -180\ \cos(\omega t) \\ 400 - 30\ \cos(\omega t) \\ 180\ \sin(\omega t) \end{bmatrix} \text{(mm)} \qquad 0 \leq t \leq 4\,T$$

where $T = 2s$ and $\omega = 2\pi/T$. In each simulation, the total time comprises four cycles. After 4 cycles, the reference signal is fixed in its last position, forcing a sudden stop. Moreover, an uncertainty level of 10% is assumed for the inertial parameters. The simulation results present a comparison between the path tracking errors in the x-, y- and z- directions, and the actuator torques. For the chosen path, the plots for the PD, PD+SM, CT and CT+SM are shown in Figs. B.2, B.3, B.4 and B.5, respectively (Appendix B).

Additionally, Table VII shows the controller parameters, while Tables VIII and IX present the obtained metrics and the steady-state errors for the chosen path. The reader can notice that the hybrid controls significantly reduce both the path tracking and steady-state errors with respect to the pure control laws, without producing a relevant increase of the actuator torques.

https://doi.org/10.1017/S0263574721000874 Published online by Cambridge University Press

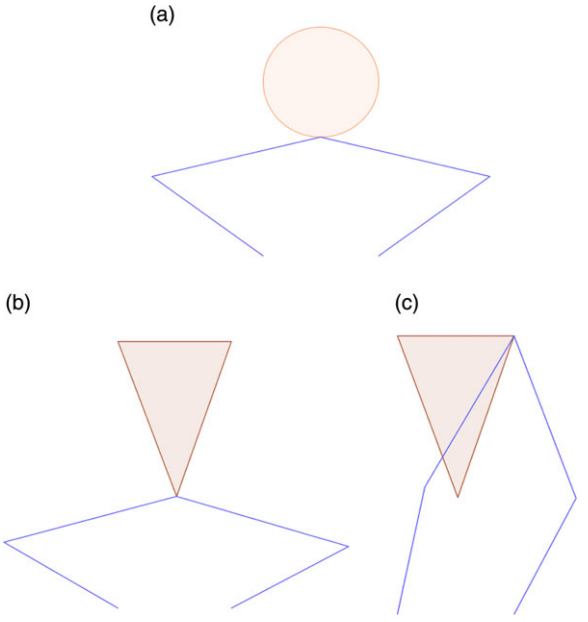


Figure 15. *(a) Circular path: initial configuration; (b) Triangular path: initial configuration; (c) Triangular path: configuration in the triangle vertex.*

5. Discussion

There are some relevant issues that need a further discussion. First, as stated before, many proposed hybrid control laws, when applied to robotic manipulators, are based on the combination of PD and Sliding Mode controls. This paper verifies experimentally the benefits of such technique, and the obtained results shows the improvement of the robot performance. On the other hand, the other tested hybrid technique, the CT+SM, demonstrates a greater performance than the PD+SM in both analysed paths.

Therefore, the model-based hybrid technique brings more benefits to the robot behaviour than the hybrid technique that is not based on its model. Furthermore, in both tested hybrid techniques, the SM was modified by adding an integration block in the control loop which effectively reduced the chattering. Moreover, another significant contribution is that this paper provides an experimental validation of the two hybrid control techniques in fast motions.

The second issue concerns on the chosen paths. The circular path is a smoother trajectory once it keeps the same angular velocity during each cycle. Hence, the robot has a continuous behaviour in a steady-state mode. On the other hand, the triangular path is a more severe trajectory, characterized by sharp curves. Then, it is possible to evaluate the robot behaviour in a transient state mode, when the robot gripper has to move from one triangle vertex to another.

Third, regarding the steady-state error, it measures the capability for reaching end positions with a certain level of precision, a requirement in pick-and-place tasks. Concerning this metric, the CT+SM hybrid technique has demonstrated an outstanding performance. With respect to the path tracking error, the other index utilized here, it constitutes a requirement in tasks such as the milling processes.

Fourth, one can observe higher tracking error in the initial configurations. For both tested paths, these errors appear only in the initial phase of the path, which might be due to static friction. For the circular path, after a while, the tracking error reduces significantly and even when it reaches that configuration in the next cycles. According to Fig. 15(a), such configuration is near an internal (type II) singularity. For the triangular path, the effect happens due to the fact that the initial configuration is the same (Fig. 15(b)). For the other triangle vertices, despite the proximity of a boundary (type I) singularity (Fig. 15(c)), low

https://doi.org/10.1017/S0263574721000874 Published online by Cambridge University Press

errors are observed. Hence, in spite of the proximity of singularities, the robot behaviour is stable in all control techniques evaluated.

Figures 7–8 show the results for the circular path when applying the pure PD and PD+SM controls, respectively. During the eight cycles, the end-effector point rotates at the same angular speed. After those cycles, the reference signal is fixed in its last position, forcing a sudden stop. The sudden stop acts as an impulsive function, and it excites all the modes of vibration of the robot structure. As the reader can notice, this behaviour does not occur for the triangular path when applying the same controls (Figs. 11–12) once the path is interpolated by a seventh-degree polynomial.

6. Conclusions

6.1. Main contributions

This paper presented two novel hybrid control laws in order to improve the dynamic behaviour of parallel robots when performing fast motion tasks. The first hybrid control resulted from the combination of a pure PD control with a modified Sliding Mode control. The second hybrid control, in its turn, combined a pure Computed Torque with the altered Sliding Mode control. The proposed modifications in the Sliding Mode control aimed to achieve a considerable reduction of the tracking errors and chattering.

In order to reveal the performance of the hybrid controls in comparison with the pure ones, experiments were conducted in a 2-dof planar parallel robot, whose end-effector performed two distinct paths. Additionally, simulations were carried out to evaluate the behaviour of a 3-dof spatial parallel robot, when performing a 3D-path.

Both the experiments and the simulations evidenced that not only the path tracking errors are significantly reduced but also the steady-state errors as well, keeping the system stability even in the proximity of singularities. In addition, the authors remark that such achievements only caused a small increase of the actuator torques with very low chattering.

Finally, the authors emphasize the feasibility of the hybrid control based on the robot model, which could be implemented in real time, and still revealed a superior behaviour in a comparison with the hybrid control not based on the robot model.

6.2. Future works

To investigate the effectiveness of hybrid techniques in redundant parallel robots, that operate in planar and three-dimensional spaces.

Acknowledgements. The authors declare no competing interests. They acknowledge grant #162502/2015-0, Conselho Nacional de Desenvolvimento Científico e Tecnológico (CNPq). The authors are also very grateful to Guilherme Scabin Vicinansa for his valuable remarks regarding the finite-time stability proof of the control law.

Supplementary Material. To view supplementary material for this article, please visit https://doi.org/10.1017/S0263574721000874.

References

[1] R. Clavel, "Robots parallles: du packaging cadence leve la production dultra haute prcision," In: Journes Nationales de la *Recherche en Robotique, 8me edn*. (2011).
[2] Physik Instrumente Group, "Hexapod +3 Redundant Measuring Systems/Legs: Medical Robot with Highest Levels of Reliability," https://www.pi-usa.us/en/news-events/hexapod-3-redundant-measuring-systems-legs (Accessed Oct 26th, 2020).
[3] PKMtricept SL, "Tricept T9000", http://www.pkmtricept.com/productos/index.php?id=en&Nproduct=1238061426 (Accessed May 26th, 2018)
[4] Starrag Group Holding AG, "Ecospeed F HT 2", https://www.starrag.com/en-us/machine/ecospeed-f-ht-2/146 (Accessed Oct 26th, 2020)

https://doi.org/10.1017/S0263574721000874 Published online by Cambridge University Press

[5] Ecorobotix Ltd., "Switch to smart weeding", https://www.ecorobotix.com/en/autonomous-robot-weeder (Accessed Oct 26th, 2020)
[6] L.-W. Tsai, *Robot Analysis: The Mechanics of Serial and Parallel Manipulators* (Wiley, New York, 1999)
[7] A. Pashkevich, D. Chablat and P. Wenger, "Kinematics and workspace analysis of a three-axis parallel manipulator: The Orthoglide," *Robotica* **24**(1), 39–49 (2006).
[8] S. Briot and I. A. Bonev, "Are parallel robots more accurate than serial robots?," *Canad. Soc. Mech. Eng. (CSME) Trans.* **31**(4), 445–456 (2007).
[9] J. Hesselbach, I. T. Pietsch, C. C. Bier and O. T. Becker, "Model-based Control of Plane Parallel Robots - How to Choose the Appropriate Approach? *Proceedings of the 4th Chemnitz Parallel Kinematics Seminar (PKS 2004), April 20–21, 2004, Chemnitz, Germany* (2004) pp. 211–232.
[10] H. B. Choi, O. Company, F. Pierrot, A. Konno, T. Shibukawa and M. Uchiyama, "Design and Control of a Novel 4-DOFs Parallel Robot H4," *IEEE International Conference on Robotics & Automation, Taipei. Proceedings. Taipei, 2003* (IEEE, 2003).
[11] H.-B. Choi, A. Konno and M. Uchiyama, "Design, implementation, and performance evaluation of a 4-DOF parallel robot," *Robotica* **28**(1), 107–118 (2010).
[12] W. Chung, L.-C. Fu and S.-H. Hsu, "Motion Control," In: *Springer Handbook of Robotics* (B. Siciliano and O. Khatib, eds.) (2008), pp. 133–159.
[13] J. J. Craig, *Introduction to Robotics: Mechanics and Control*, 4th edn. (Pearson, London, UK, 2017).
[14] J.-J.E. Slotine, "The robust control of robot manipulators," *Int. J. Rob. Res.* **4**(2), 49–64 (1985).
[15] Z. Zhan, X. Zhang, Z. Jian and H. Zhang, "Error modelling and motion reliability analysis of a planar parallel manipulator with multiple uncertainties," *Mech. Mach. Theory* **124**(June), 55–72 (2018).
[16] D. Grzelczyk, B. Staczyk and J. Awrejcewicz, "Prototype, control system architecture and controlling of the hexapod legs with nonlinear stick-slip vibrations," *Mechatronics* **37**(August), 63–78 (2016).
[17] A. Zubizarreta, I. Cabanes, M. Marcos and C. Pinto, "A redundant dynamic model of parallel robots for model-based control," *Robotica* **31**(2), 203–216 (2013).
[18] Y. Singh and M. Santhakumar, "Inverse dynamics and robust sliding mode control of a planar parallel (2-PRP and 1-PPR) robot augmented with a nonlinear disturbance observer," *Mech. Mach. Theory* **92**(October), 29–50 (2015).
[19] E. Ozgur, N. Andreff and P. Martinet, "Vector-Based Dynamic Modeling and Control of the Quattro Parallel Robot by Means of Leg Orientations," 2010 *IEEE International Conference on Robotics and Automation Anchorage Convention District May 3–8, 2010, Anchorage, Alaska, USA* (2010).
[20] Y. Li and Q. Xu, "Dynamic modeling and robust control of a 3-PRC translational parallel kinematic machine," *Rob. Comput. Integr. Manuf.* **25**(3), 630–640 (2009).
[21] S. Mohan, "Error analysis and control scheme for the error correction in trajectory-tracking of a planar 2PRP-PPR parallel manipulator," *Mechatronics* **46**(October), 70–83 (2017).
[22] D. Wang, J. Wu, L. Wang, Y. Liu and G. Yu, "A method for designing control parameters of a 3-DOF parallel tool head," *Mechatronics* **41**(February), 102–113 (2017).
[23] K. Lipiski, "Modeling and control of a redundantly actuated variable mass 3RRR planar manipulator controlled by a model-based feedforward and a model-based-proportional-derivative feedforwardfeedback controller," *Mechatronics* **37**(August), 42–53 (2016).
[24] M. G. Safonov, "Origins of robust control: Early history and future speculations," *Ann. Rev. Control* **36**(2), 173–181 (2012).
[25] S. Islam and X. P. Liu, "Robust sliding mode control for robot manipulators," *IEEE Trans. Ind. Electr.* **58**(6), 2444–2453 (2011).
[26] B. Achili, B. Daachi, Y. Amirat, A. Ali-Cherif and M.E. Dachi, "A stable adaptive force/position controller for a C5 parallel robot: A neural network approach," *Robotica* **30**(7), 1177–1187 (2012).
[27] F. Piltan and N. B. Sulaiman, "Review of sliding mode control of robotic manipulator," *World Appl. Sci. J.* **18**(12), 1855–1869 (2012).
[28] A. Chevalier, C. Copot, C. M. Ionescu and R. De Keyser, "Automatic calibration with robust control of a six DoF mechatronic system," *Mechatronics* **35**(May), 102–108 (2016).
[29] J. Shi, H. Liu and N. Bajcinca, "Robust control of robotic manipulators based on integral sliding mode," *Int. J. Control* **81**(10), 1537–1548 (2008).
[30] J. M. Daly and H. M. Schwartz, "Experimental results for output feedback adaptive robot control," *Robotica* **24**(6), 727–738 (2006).
[31] G. S. Natal, A. Chemori and F. Pierrot, "Nonlinear control of parallel manipulators for very high accelerations without velocity measurement: Stability analysis and experiments on Par2 parallel manipulator," *Robotica* **34**(1), 43–70 (2016).
[32] M. Zeinali and L. Notash, "Adaptive sliding mode control with uncertainty estimator for robot manipulators," *Mech. Mach. Theory* **45**(1), 80–90 (2010).
[33] B. K. Sarkar, "Modeling and validation of a 2-DOF parallel manipulator for pose control application," *Rob. Comput. Integr. Manuf.* **50**(April), 234–241 (2018).
[34] Y. Long, Z. J. Du, W. D. Wang and W. Dong, "Robust sliding mode control based on GA optimization and CMAC compensation for lower limb exoskeleton," *Appl. Bionics Biomech.* 2016, Article ID 5017381, 13 p (2016).
[35] M. Mahmoodabadi, M. Taherkhorsandi, M. Talebipour and K. Castillo-Villar, "Adaptive robust PID control subject to supervisory decoupled sliding mode control based upon genetic algorithm optimization," *Trans. Inst. Meas. Control* **37**(4), 505–514 (2015).

https://doi.org/10.1017/S0263574721000874 Published online by Cambridge University Press

[36] K. J. Lee, J. J. Choi and J. S. Kim, "A proportional-derivative-sliding mode hybrid control scheme for a robot manipulator," *Proc. Inst. Mech. Eng. Part I J. Syst. Control Eng.* **218**(8), 667–674 (2004).
[37] S. Li, A. Ghasemi, W. Xie and Y. Gao, "An enhanced IBVS controller of a 6DOF manipulator using hybrid PD-SMC method," *Int. J. Control Autom. Syst.* **16**(April), 844–855 (2018).
[38] H.-V.-A. Truong, D.-T. Tran and K. K. Ahn, "A neural network based sliding mode control for tracking performance with parameters variation of a 3-DOF manipulator," *Appl. Sci.* **9**(10), 2023 (2019).
[39] J. M. Acob, V. Pano and P. R. Ouyang, "Hybrid PD Sliding Mode Control of a Two-Degree-of-Freedom Parallel Robotic Manipulator," *10th IEEE International Conference on Control and Automation (ICCA) Hangzhou, China, June 12–14, 2013* (2013) pp. 1760–1765.
[40] J. M. Acob, Hybrid PD Sliding Mode Control for Robotic Manipulators *MSc Thesis* (Ryerson University, Canada, 2015).
[41] T. Kara, and A. L. Mary, "Adaptive PD-SMC for nonlinear robotic manipulator," *Tracking Control Stud. Inf. Control* **26**(1), 49–58 (2017).
[42] F.-J. Lin and R.-J. Wai, "Hybrid Computed Torque controlled motortoggle servomechanism using fuzzy neural network uncertainty observer," *Neurocomputing* **48**(October), 403–422 (2002).
[43] H. Yu, "Modeling and control of hybrid machine systems - a five-bar mechanism case," *Int. J. Autom. Comput.* **3**(July), 235–243 (2006).
[44] J. Peng, J. Wang and Y. Wang, "Neural network based robust hybrid control for robotic system: An H∞ approach," *Nonlinear Dyn.* **65**(September), 421–431 (2011).
[45] C. Roldn-Paraponiaris, F. J. Campa and O. Altuzarra, "Mechatronic modeling of a parallel kinematics multi-axial simulation table based on decoupling the actuators and manipulator dynamics," *Mechatronics* **47**(November), 208–222 (2017).
[46] B. Olofsson and L. Nielsen, "Path-tracking velocity control for robot manipulators with actuator constraints," *Mechatronics* **45**(August), 82–99 (2017).
[47] S. Wen, X. Hu, B. Zhang, M. Sheng, H. K. Lam and Y. Zhao, "Fractional-order internal model control algorithm based on the force/position control structure of redundant actuation parallel robot," *Int. J. Adv. Rob. Syst.* **17**(1), 1–13 (2020).
[48] Q. Li, "Experimental validation on the integrated design and control of a parallel robot," *Robotica* **24**(2), 173–181 (2006).
[49] A. G. Coutinho, V. P. Bartholomeu, I. Stevanni, J. M. Oliveira-Fuess, T. A. Hess-Coelho and D. Colon, "Design and Control of 2-DOF Parallel Mechanism," *25th ABCM International Congress of Mechanical Engineering, October 20-25, Uberlandia, Brazil* (2019).
[50] H. Zhang, H. Fang and Q. Zou, "Non-singular terminal sliding mode control for redundantly actuated parallel mechanism," *Int. J. Adv. Rob. Syst.* **17**(2), 1–13 (2020).
[51] W. Khalil and E. Dombre, *Modeling, Identification and Control of Robots* (Hermes Penton Ltd., 2002).
[52] Z. Qi, J. E. McInroy and F. Jafari, "Trajectory tracking with parallel robots using low chattering, fuzzy sliding mode controller," *J. Intell. Rob. Syst.* **48**(March), 333–356 (2007).
[53] C. Suttirak and C. Pukdeboon, "Finite-time convergent sliding mode controllers for robot Ma- nipulators," *Appl. Math. Sci.* **7**(63), 3141–3154 (2013).
[54] Z. Chen, X. Yang, X. Zhang and P. X. Liu, Finite-time trajectory tracking control for rigid 3-DOF manipulators with disturbances. doi: 10.1109/ACCESS.2018.2859435.
[55] M. T. Thompson, *Intuitive Analog Circuit Design*, 2nd edn. (Elsevier, Oxford, UK, 2014)
[56] R. M. M. Orsino and T. A. Hess-Coelho, "A contribution on the modular modelling of multibody systems," *Proc. R. Soc. A* **471**(2183), 20150080 (2015). doi: 10.1098/rspa.2015.0080.
[57] T. A. Hess-Coelho, R. M. M. Orsino and F. Malvezzi, "Modular modelling methodology applied to the dynamic analysis of parallel mechanisms," *Mech. Mach. Theory* **161**(July), 104332 (2021).

Appendix A. Dynamic model of a 2-dof planar mechanism 5R

The development of the dynamic model of a 2-dof planar 5R mechanism (Fig. 3) follows the approach of the Modular Modelling Methodology [56, 57]. Consider the i-th kinematic chain of the parallel mechanism, composed of the links 1 and 2. The unit vectors of the frame attached to the first link are

$$^{0}\mathbf{i}_{i_1} = \cos\theta_{i,1}\mathbf{i}_0 + \sin\theta_{i,1}\,\mathbf{j}_0$$

$$^{0}\mathbf{j}_{i_1} = -\sin\theta_{i,1}\mathbf{i}_0 + \cos\theta_{i,1}\,\mathbf{j}_0 \qquad ^{0}\mathbf{k}_{i_1} = \mathbf{k}_0$$

The vectors of the angular velocity of link 1 and the velocity of the centre of mass G_1 are, respectively,

$$\boldsymbol{\omega}_{i,1} = \dot{\theta}_{i,1}\,\mathbf{k}_{i_1} = \omega_{i,1}\mathbf{k}_{i_1} \qquad \mathbf{v}_{G_{i_1}} = \omega_{i,1}\,\ell_{i_{g1}}\,\mathbf{j}_{i_1}$$

Those vectors can be rewritten as follows,

$$\mathbf{v}_{G_{i_1}} = V_{i_1}\,\boldsymbol{\omega}_i \qquad \omega_{i,1} = \Omega_{i_1}\,\boldsymbol{\omega}_i$$

https://doi.org/10.1017/S0263574721000874 Published online by Cambridge University Press

where

$$\boldsymbol{\omega}_i = [\omega_{i,1},\ \omega_{i,2}]^T \qquad V_{i_1} = \begin{bmatrix} \dfrac{\partial \mathbf{v}_{G_{i_1}}}{\partial \omega_{i,1}} & \dfrac{\partial \mathbf{v}_{G_{i_1}}}{\partial \omega_{i,2}} \end{bmatrix} \qquad \Omega_{i_1} = \begin{bmatrix} \frac{\partial \boldsymbol{\omega}_{i,1}}{\partial \omega_{i,1}} & \dfrac{\partial \boldsymbol{\omega}_{i,1}}{\partial \omega_{i,2}} \end{bmatrix}$$

Hence,

$$V_{i_1} = \begin{bmatrix} \ell_{i_{g1}} \mathbf{j}_{i_1} & \mathbf{0} \end{bmatrix} = \begin{bmatrix} 0 & 0 \\ \ell_{i_{g1}} & 0 \end{bmatrix} \qquad \Omega_{i_1} = \begin{bmatrix} 1 & 0 \end{bmatrix}$$

Moreover, the inertia forces of the first link can be calculated as follows,

$$m_{i_1} \mathbf{a}_{G_{i_1}} = m_{i_1}(\dot{V}_{i_1} \boldsymbol{\omega}_i + V_{i_1}\, \dot{\boldsymbol{\omega}}_i) \qquad J_{i_{z1}}\, \dot{\omega}_{i,1} = J_{i_{z1}}\, \Omega_{i_1}\, \dot{\boldsymbol{\omega}}_i$$

where

$$\dot{V}_{i_1} = \begin{bmatrix} -\ell_{i_{g1}} \omega_{i,1}\, \mathbf{i}_{i_1} & \mathbf{0} \end{bmatrix} = \begin{bmatrix} -\ell_{i_{g1}} \omega_{i,1} & 0 \\ 0 & 0 \end{bmatrix}$$

The unit vectors of the frame attached to the second link are

$${}^0\mathbf{i}_{i_2} = \cos(\theta_{i,1} + \theta_{i,2})\mathbf{i}_0 + \sin(\theta_{i,1} + \theta_{i,2})\mathbf{j}_0$$

$${}^0\mathbf{j}_{i_2} = -\sin(\theta_{i,1} + \theta_{i,2})\mathbf{i}_0 + \cos(\theta_{i,1} + \theta_{i,2})\mathbf{j}_0 \qquad {}^0\mathbf{k}_{i_2} = \mathbf{k}_0$$

The vectors of the angular velocity of link 2 and the velocity of the centre of mass G_2 are, respectively,

$$\boldsymbol{\omega}_{i,2} = (\dot{\theta}_{i,1} + \dot{\theta}_{i,2})\, \mathbf{k}_{i_2} = \omega_{i,2}\, \mathbf{k}_{i_2} \qquad \mathbf{v}_{G_{i_2}} = \omega_{i,1}(\ell_1)\, \mathbf{j}_{i_1} + \omega_{i,2} \ell_{i_{g2}}\, \mathbf{j}_{i_2}$$

Those vectors can be rewritten as follows,

$$\mathbf{v}_{G_{i_2}} = V_{i_2}\, \boldsymbol{\omega}_i \qquad \omega_{i,2} = \Omega_{i_2}\, \boldsymbol{\omega}_i$$

where

$$V_{i_2} = \begin{bmatrix} \ell_1\, \mathbf{j}_{i_1} & \ell_{i_{g2}}\, \mathbf{j}_{i_2} \end{bmatrix} = \begin{bmatrix} \ell_1 {}^2R_1\, {}^1\mathbf{j}_{i_1} & \ell_{i_{g2}} {}^2\mathbf{j}_{i_2} \end{bmatrix} \qquad \Omega_{i_2} = \begin{bmatrix} 0 & 1 \end{bmatrix}$$

$${}^2R_1 = \begin{bmatrix} \cos\theta_{i,2} & \sin\theta_{i,2} \\ -\sin\theta_{i,2} & \cos\theta_{i,2} \end{bmatrix}$$

Hence,

$$V_{i_2} = \begin{bmatrix} \ell_1\ \sin\theta_{i,2} & 0 \\ \ell_1\ \cos\theta_{i,2} & \ell_{i_{g2}} \end{bmatrix}$$

Moreover, the inertia forces of the second link can be calculated as follows,

$$m_{i_2} \mathbf{a}_{G_{i_2}} = m_{i_2}(\dot{V}_{i_2} \boldsymbol{\omega}_i + V_{i_2} \dot{\boldsymbol{\omega}}_i) \qquad J_{i_{z2}}\, \dot{\omega}_{i,2} = J_{i_{z2}}\, \Omega_{i_2}\, \dot{\boldsymbol{\omega}}_i$$

where

$$\dot{V}_2 = \begin{bmatrix} -\ell_1 \omega_{i,1}\, {}^2\mathbf{i}_{i_1} & -\ell_{i_{g2}} \omega_{i,2}\, {}^2\mathbf{i}_{i_2} \end{bmatrix} = \begin{bmatrix} -\ell_1\ \cos\theta_{i,2}\, \omega_{i,1} & -\ell_{i_{g2}}\, \omega_{i,2} \\ \ell_1\ \sin\theta_{i,2}\, \omega_{i,1} & 0 \end{bmatrix}$$

The vector of the velocity of point E, the centre of the revolute joint that connects the first kinematic chain with the second one, can be computed as follows,

$$\mathbf{v}_E = \dot{x}_E\, \mathbf{i}_0 + \dot{y}_E\, \mathbf{j}_0$$

https://doi.org/10.1017/S0263574721000874 Published online by Cambridge University Press

For the i-th kinematic chain, the vector $\mathbf{v}_E$ can also be calculated by using either the vector notation,

$$\mathbf{v}_E = \ell_1 \omega_{i,1}\, \mathbf{j}_{i_1} + \ell_2 \omega_{i,2}\, \mathbf{j}_{i_2}$$

or the matricial notation,

$$\mathbf{v}_E = \begin{bmatrix} \ell_1{}^0\mathbf{j}_{i_1} & \ell_2{}^0\mathbf{j}_{i_2} \end{bmatrix} \boldsymbol{\omega}_i = \begin{bmatrix} -\ell_1 \sin\theta_{i,1} & -\ell_2 \sin(\theta_{i,1}+\theta_{i,2}) \\ \ell_1 \cos\theta_{i,1} & \ell_2 \cos(\theta_{i,1}+\theta_{i,2}) \end{bmatrix} \boldsymbol{\omega}_i = J_{w_i}\ \boldsymbol{\omega}_i$$

Moreover, the differentiation of the vector $\mathbf{v}_E$ with respect to time is

$$\dot{\mathbf{v}}_E = \dot{J}_{w_i}\ \boldsymbol{\omega}_i + J_{w_i}\ \dot{\boldsymbol{\omega}}_i$$

Hence, the vector of the angular acceleration $\dot{\boldsymbol{\omega}}_i$ is

$$\dot{\boldsymbol{\omega}}_i = C_i\ (\ \dot{\mathbf{v}}_E - \dot{J}_{w_i}\ \boldsymbol{\omega}_i\ )$$

where

$$C_i\ = J_{w_i}^{-1}$$

Additionally, the dot product of the vector $\mathbf{i}_2$ by the vector $\dot{\mathbf{x}}$ is

$$\mathbf{i}_{i_2}^T\, \mathbf{v}_E = \ell_1\, \mathbf{i}_{i_2}^T\, \mathbf{j}_{i_1}\, \omega_{i,1} + \ell_2\, \mathbf{i}_{i_2}^T\, \mathbf{j}_{i_2}\, \omega_{i,2} = \ell_1\, \mathbf{i}_{i_2}^T\, \mathbf{j}_{i_1}\, \omega_{i,1}$$

Therefore,

$$J_E\ \mathbf{v}_E = J_\theta\ \dot{\boldsymbol{\theta}}$$

where

$$\dot{\boldsymbol{\theta}} = [\omega_{1,1},\ \omega_{2,1}]^T$$

$$J_E = \begin{bmatrix} \mathbf{i}_{1_2}^T \\ \mathbf{i}_{2_2}^T \end{bmatrix} = \begin{bmatrix} \cos(\theta_{1,1}+\theta_{1,2}) & \sin(\theta_{1,1}+\theta_{1,2}) \\ \cos(\theta_{2,1}+\theta_{2,2}) & \sin(\theta_{2,1}+\theta_{2,2}) \end{bmatrix}$$

$$J_\theta = \ell_1 \begin{bmatrix} \mathbf{i}_{1_2}^T\, \mathbf{j}_{1_1} & 0 \\ 0 & \mathbf{i}_{2_2}^T\, \mathbf{j}_{2_1} \end{bmatrix} = \ell_1 \begin{bmatrix} \sin\theta_{1,2} & 0 \\ 0 & \sin\theta_{2,2} \end{bmatrix}$$

By assuming the variables $\theta_{1,1}$ and $\theta_{2,1}$ as the independent coordinates, the dynamic model of the 2-dof planar 5R mechanism can be expressed by the following equation

$$\mathbf{H}(\boldsymbol{\theta})\, \ddot{\boldsymbol{\theta}} + \boldsymbol{h}(\boldsymbol{\theta}, \dot{\boldsymbol{\theta}}) = \boldsymbol{u}$$

For the whole mechanism, the inertia matrix $\mathbf{H}(\boldsymbol{\theta})$ can be calculated as

$$\mathbf{H}(\boldsymbol{\theta}) = D^T(\mathbb{M}_1 + \mathbb{M}_2)\, D$$

where

$$D = J_E^{-1} J_\theta \qquad \mathbb{M}_1 = C_1^T \left(\sum_{k=1}^{2} V_{1_k}^T m_{1_k} V_{1_k} + \Omega_{1_k}^T J_{1_{zk}}\ \Omega_{1_k} \right) C_1$$

$$\mathbb{M}_2 = C_2^T \left(\sum_{k=1}^{2} V_{2_k}^T m_{2_k} V_{2_k} + \Omega_{2_k}^T J_{2_{zk}}\ \Omega_{2_k} \right) C_2$$

https://doi.org/10.1017/S0263574721000874 Published online by Cambridge University Press

Moreover, the term $\boldsymbol{h}(\boldsymbol{\theta}, \dot{\boldsymbol{\theta}})$ takes into account the efforts due to the centripetal and Coriolis effects,

$$\boldsymbol{h}(\boldsymbol{\theta}, \dot{\boldsymbol{\theta}}) = D^T(\mathbb{H}_1 + \mathbb{H}_2) + D^T(\mathbb{M}_1 + \mathbb{M}_2)\dot{D}\ \dot{\boldsymbol{\theta}}$$

where

$$\mathbb{H}_1 = C_1^T \left[\left(\sum_{k=1}^{2} V_{1_k}^T m_{1_k} V_{1_k} + \Omega_{1_k}^T J_{1_{z}k}\ \Omega_{1_k} \right) (-C_1 \dot{J_{w_1}}) + \sum_{k=1}^{2} V_{1_k}^T m_{1_k} \dot{V}_{1_k} \right] \boldsymbol{\omega}_1$$

$$\mathbb{H}_2 = C_2^T \left[\left(\sum_{k=1}^{2} V_{2_k}^T m_{2_k} V_{2_k} + \Omega_{2_k}^T J_{2_{z}k}\ \Omega_{2_k} \right) (-C_2 \dot{J_{w_2}}) + \sum_{k=1}^{2} V_{2_k}^T m_{2_k} \dot{V}_{2_k} \right] \boldsymbol{\omega}_2$$

Finally, the term $\boldsymbol{u}$ considers the actuator torques $\tau_{1,1}$ and $\tau_{2,1}$,

$$\boldsymbol{u} = D^T(\mathbb{T}_1 + \mathbb{T}_2)$$

where

$$\mathbb{T}_1 = C_1^T\ \Omega_{1_1}^T\ (\tau_{1,1} + \tau_{f_1}) \qquad \mathbb{T}_2 = C_2^T\ \Omega_{2_1}^T\ (\tau_{2,1} + \tau_{f_2})$$

and

$$\tau_{f_1} = -b_1\,\omega_{1,1} - \mu_1\,\mathrm{sgn}(\omega_{1,1}) \qquad \tau_{f_2} = -b_2\,\omega_{2,1} - \mu_2\,\mathrm{sgn}(\omega_{2,1})$$

Appendix B. Results from the simulations

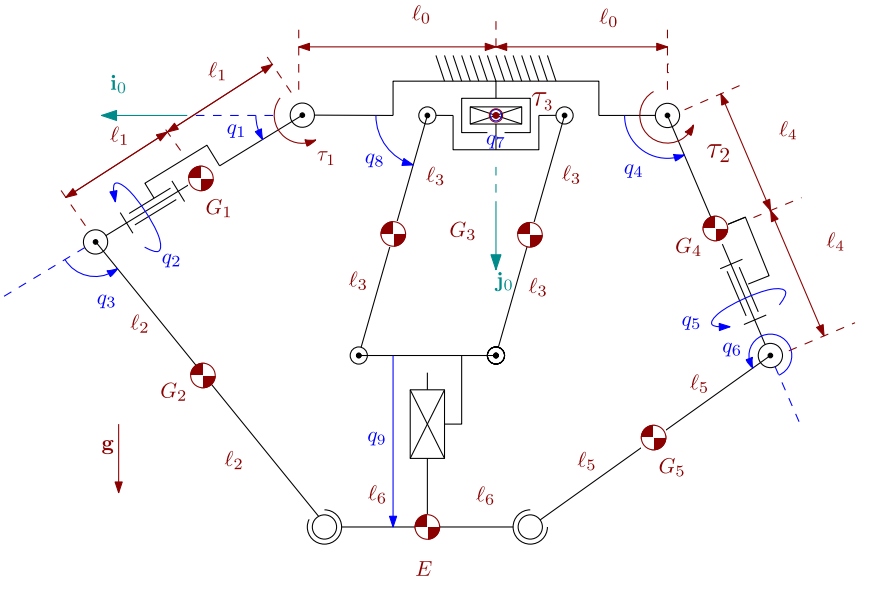


Figure B.1. *The 2RRRS+P(Pa)P: representation of the mechanical structure, variables, parameters, centres of mass and actuator torques/force.*

https://doi.org/10.1017/S0263574721000874 Published online by Cambridge University Press

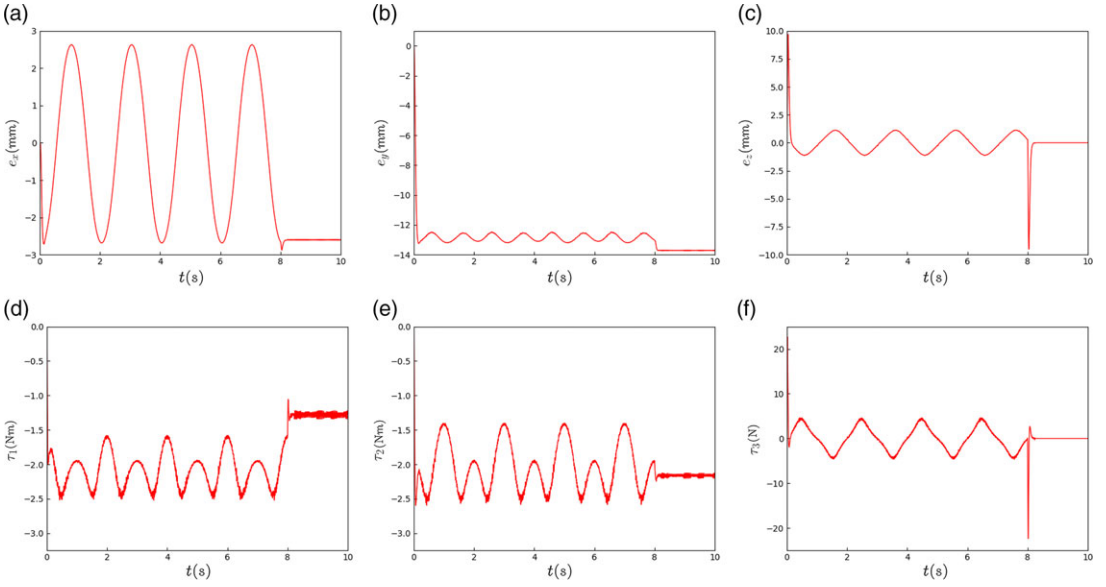


Figure B.2. *Pure PD control: spatial parallel robot simulation. (a) x-direction control error. (b) y-direction control error. (c) z-direction control error. (d) Torque of actuator 1. (e) Torque of actuator 2. (f) Force of actuator 3.*

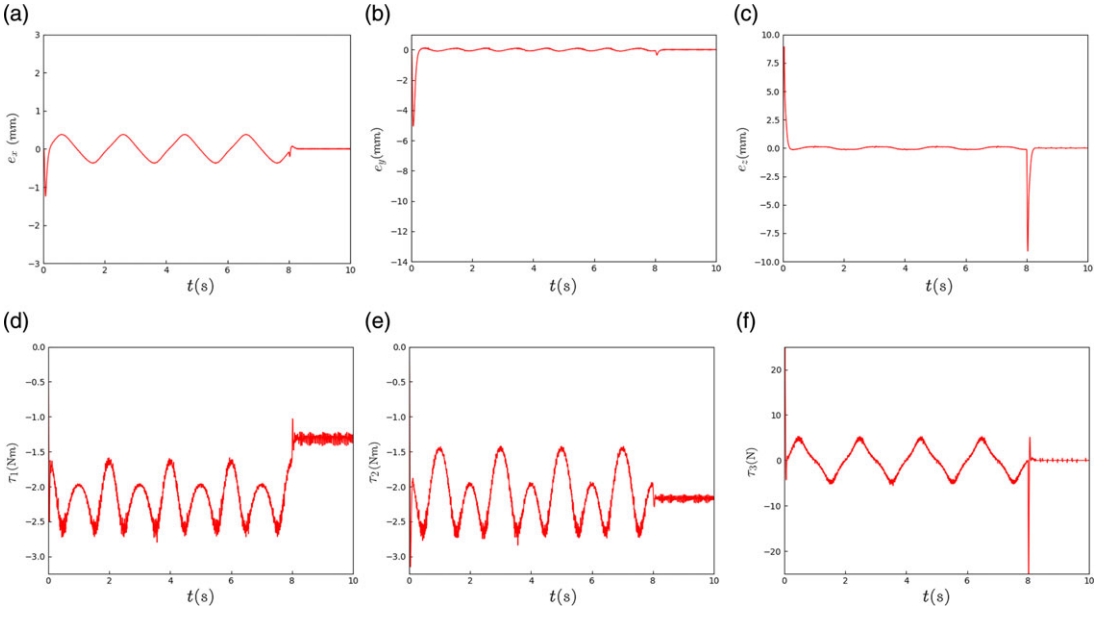


Figure B.3. *Hybrid PD+SM control: spatial parallel robot simulation. (a) x-direction control error. (b) y-direction control error. (c) z-direction control error. (d) Torque of actuator 1. (e) Torque of actuator 2. (f) Force of actuator 3.*

https://doi.org/10.1017/S0263574721000874 Published online by Cambridge University Press

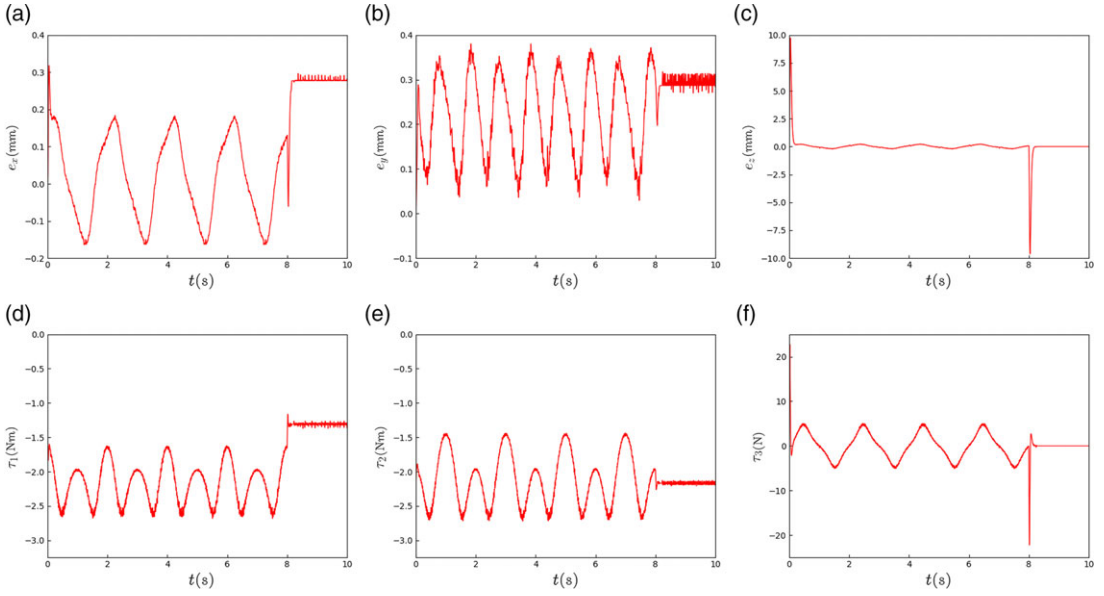


Figure B.4. *Pure CT control: spatial parallel robot simulation. (a) x-direction control error. (b) y-direction control error. (c) z-direction control error. (d) Torque of actuator 1. (e) Torque of actuator 2. (f) Force of actuator 3.*

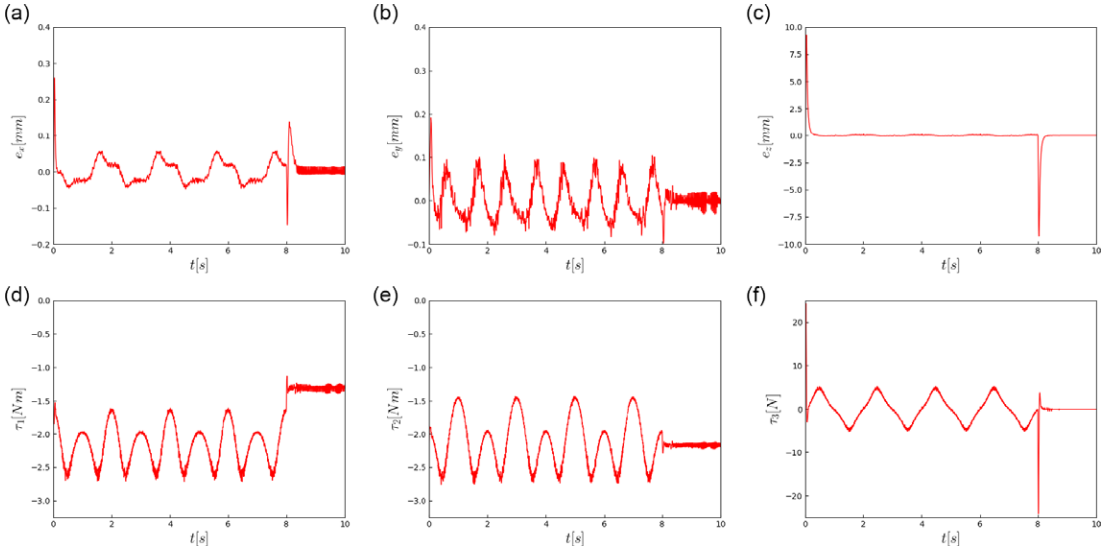


Figure B.5. *Hybrid CT+SM control: spatial parallel robot simulation. (a) x-direction control error. (b) y-direction control error. (c) z-direction control error. (d) Torque of actuator 1. (e) Torque of actuator 2. (f) Force of actuator 3.*

https://doi.org/10.1017/S0263574721000874 Published online by Cambridge University Press

Table B.1. *Robot parameters: lengths, masses and central mass moments of inertia of the links.*

Link *i*	l_i **(mm)**	m_i **(kg)**	I_x **(kg m^2)**	I_y **(kg m^2)**	I_z **(kg m^2)**
0	260	–	–	–	–
1(G_1)	172.5	0.275	0	0	4.832×10^{-3}
2(G_2)	220	0.050	50×10^{-6}	15×10^{-6}	50×10^{-6}
3(G_3)	192.5	0.461	0	0	9.218×10^{-3}
4(G_4)	172.5	0.275	0	0	4.832×10^{-3}
5(G_5)	220	0.050	50×10^{-6}	15×10^{-6}	50×10^{-6}
6(E)	80	0.378	–	–	–

Cite this article: A. G. Coutinho and T. A. Hess-Coelho (2022). "Improving the performance of parallel robots by applying distinct hybrid control techniques", Robotica **40**, 951–975. https://doi.org/10.1017/S0263574721000874
https://doi.org/10.1017/S0263574721000874 Published online by Cambridge University Press